



Hydroxyapatite and Whitlockite Incorporated Cellulose Reinforced Poly-Caprolactone (PCL): Biomimetic Nanocomposites for Bone Tissue Engineering Applications

Laraib Abbas¹ · Farzana Nazir¹ · Asma Gulzar¹ · Laiba Maryam¹ · Asima Tayyeb² · Mudassir Iqbal¹

Accepted: 5 December 2022 / Published online: 20 December 2022

© The Author(s), under exclusive licence to Springer Science+Business Media, LLC, part of Springer Nature 2022

Abstract

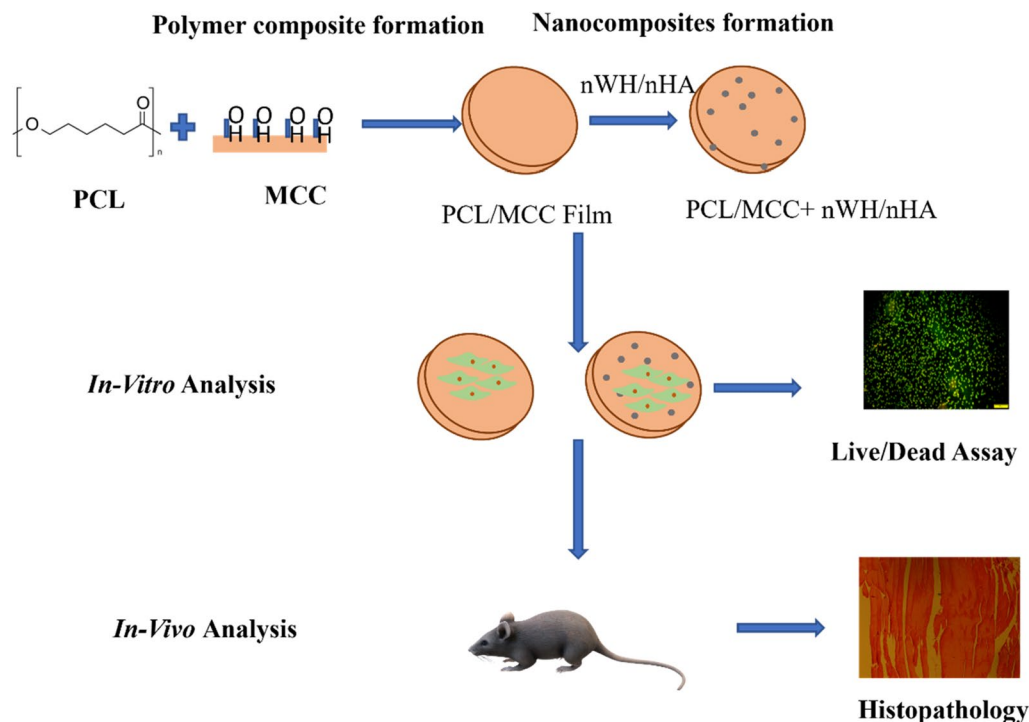
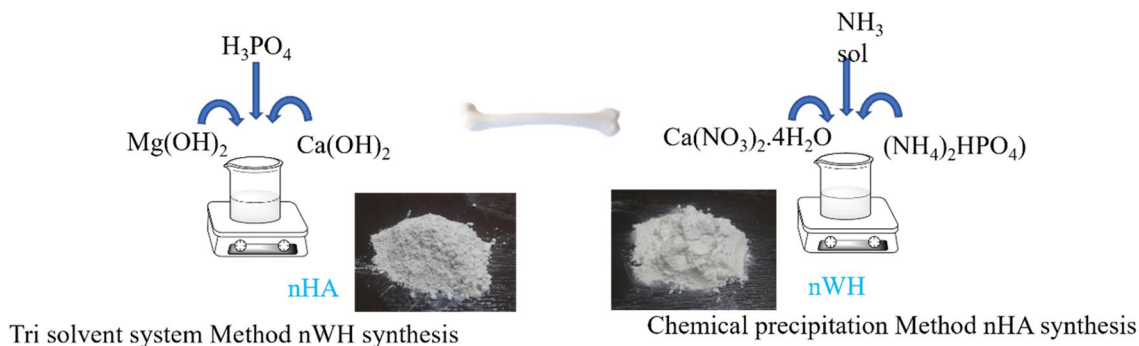
Structure-activity relationship of nano-hydroxyapatite (nHA) and whitlockite (nWH) nanocomposites using Poly-Caprolactone (PCL) and Microcrystalline cellulose (MCC) composite (95/5, 90/10, 85/15 wt%) for bone tissue regeneration is elucidated in this report. Morphology, crystallinity, thermal properties, degradation, mechanical properties, and In Vitro, In Vivo biocompatibility of composites were systematically evaluated. Briefly, nHA and nWH nanoparticles were synthesized by chemical precipitation and trisolvant systems, respectively. MCC 5 wt% in PCL matrix (PCL/MCC-5) showed enhanced mechanical strength, increased crystallinity, and porous morphology compared to virgin PCL. Morphological analysis of nHA and nWH reinforced PCL/MCC-5 composite revealed a reduction in the pore size. Structural analysis, XRD, FTIR, and DSC concluded that nHA and nWH addition (1–10 wt%) improved the crystallinity of the PCL/MCC-5 by acting as nucleating sites for polymer chains. The presence of Van der Waals forces of attraction caused an increase in crystallinity and a decrease in pore size. Mechanical testing revealed an increase in modulus by 113 times for 10 wt% nHA and 125 times increase on 10 wt% nWH loading compared to virgin PCL. In vitro cytocompatibility using Vero cell line showed ~88% cell viability for PCL/MCC-5 composite and ~94% for 5wt% and 10 wt% nHA loaded composite on day 7, which shows nanoparticles improved osteoconductive and osteoinductivity of the composites. LIVE/DEAD assay with NIH3T3-L1 cell lines with 1% nHA showed the highest cell viability for all 3, 7, 14, and 21 days. In vivo trials with 10 wt% of nHA and nWH demonstrated full and thick muscle adherence and bio-interfacial affinity to the nanocomposites in comparison to virgin PCL. Our findings suggest that PCL/MCC composite with nHA and nWH may serve as a promising bone implant.

✉ Mudassir Iqbal
mudassir.iqbal@sns.nust.edu.pk

¹ Department of Chemistry, School of Natural Sciences, National University of Sciences and Technology (NUST), Islamabad 44000, Pakistan

² School of Biological Sciences, University of the Punjab, Lahore, Pakistan

Graphical Abstract



Keywords Poly-caprolactone · Microcrystalline cellulose · Hydroxyapatite · Whitlockite · Mechanical properties · Degradation bone tissue engineering

Introduction

Despite the inherent self-regeneration capacity of bone, certain congenital disorders and non-union fractures accompanied by trauma, infection, or injury exceed the critical self-repairing limit. They can lead to permanent loss or dysfunction of osseous tissues [1]. Previously, these skeletal defects have been amended by autografts (gold standard), allografts, and xenografts. But these approaches suffer from substantial limitations such as two-site surgery,

disease transmission, donor site morbidity, and immune system denunciation. Metal and ceramic-based bone grafts can also be inserted to aid bone repair. However, their intrinsic disadvantages include bone thinning, lack of degradability, and processability, which confine their applications [2].

To surmount these limitations, researchers are directed toward seeking new alternatives to traditional treatment methods. In recent decades, bone tissue engineering (BTE) has come to the fore [3], which is mainly focused on developing porous scaffolds which can be implanted into defect

sites. In addition to porosity, osteoconductivity, biocompatibility, biodegradability, immunogenicity, and excellent mechanical strength are qualities of an ideal scaffold [4–7]. The principle of BTE is to utilize scaffolds or synthetic extracellular matrix along with osteoblast and growth factors to bring about cell recruitment, proliferation, and differentiation [8]. Porous scaffolds act as templates and facilitate cell seeding and bone tissue formation. No ideal scaffold material has been encountered yet, but polymers make an attractive and promising bone substitute formation. The enormous growth in polymeric composite has been witnessed over the last few years in their biomedical applications [9–12]. The bio-artificial blending of polymers involves the mixing of synthetic and natural polymers to impart exceptional mechanical and structural properties to scaffolds [9, 13, 14].

Poly-caprolactone (PCL) has garnered much attention in biomaterial engineering [15, 16]. PCL is an aliphatic polyester, semi-crystalline in nature, and possesses high solubility in chlorinated solvents and low melting point, making its processing and blending with polymer materials facile [17]. Its biocompatibility, permeability, easy manipulation, and US Food and Drug Authority (FDA) approval make it a potential candidate to make artificial constructs [18, 19]. However, slow resorption rate, hydrophobicity, mechanical stability and non-osteogenic nature limit its application [17, 19]. To better cater to the necessities of the host cells. Microcrystalline cellulose (MCC) is incorporated into PCL, fine-tuning the biodegradation rate. MCC, the most abundant polymer serves as a counterpart of collagen, supports osteo differentiation, and provides a cellular milieu [20, 21] it can be implicated in bone implants [22].

Nanoparticles are widely used in medical applications [23, 24] and other advanced fields [25–28]. Addition of nanoparticle in polymers leads to the polymeric nanocomposites which have synergistic combination of beneficial properties of the polymer and nanoparticles [12, 22–24, 29]. While to improve the osteoinductive, osteoconductive character of the scaffolds, incorporating ceramics such as (nano-hydroxyapatite) nHA and nWH (nano-whitlockite) is a practical approach. HA and WH are the most abundant inorganic phases in the skeletal tissues, respectively [30]. They emulate natural bone and are dispersed in the collagen matrix, making bone a true nanocomposite [31, 32]. WH imitates bone remodeling by inhibiting monocyte's conversion to osteoclasts, regulating osteogenic differentiation and transforming into HA [33, 34]. HA can also transform into WH and is the only calcium phosphate compound thermodynamically stable at neutral pH. Regulated architecture and biomaterial properties are the indispensable features required to mimic the osseous tissues.

Herein, we account for lab synthesis of nHA, nWH, and PCL/MCC polymeric composite. Then we fabricated biomimetic nanocomposites in which nHA and nWH are

embedded in PCL/MCC composite in different weight ratios. Furthermore, a comparative study was carried out on the structural and thermomechanical properties of composite and nanocomposites. In vivo profiles of composite and nHA and nWH-based nanocomposites were evaluated to understand nanocomposites bone tissue regeneration potential, using Vero cell lines and NIH3T3 cell lines. to understand nanocomposites bone tissue regeneration potential.

Materials and Methods

Materials

Poly-Caprolactone (Mn: number average Molecular mass $70,000 \text{ g mol}^{-1}$) was obtained from Polysciences, Inc. USA. Microcrystalline Cellulose (MCC) (20–100 μm), was obtained from DAEJUNG Co., LTD, South Korea. Chloroform research grade (99% pure) were procured from Sigma Aldrich Co., USA. Di-Ammonium hydrogen phosphate, $(\text{NH}_4)_2\text{HPO}_4$, ¹ (98%), Calcium nitrate tetrahydrate, $\text{Ca}(\text{NO}_3)_2 \cdot 4\text{H}_2\text{O}$, (complexometric assay $\geq 100\%$), Calcium hydroxide, $\text{Ca}(\text{OH})_2 \geq (85\%)$, Magnesium hydroxide, $\text{Mg}(\text{OH})_2$, 85%, Ammonia Solution, $\text{NH}_3 \text{ sol}$, (35%), Phosphoric Acid (H_3PO_4) 85%, and Deionized water from Fisher Scientific International, Inc. USA were acquired and utilized as such.

Synthesis of Hydroxyapatite Nanoparticles (nHA)

Hydroxyapatite nanoparticles (nHA) were synthesized by combining calcium nitrate tetrahydrate ($\text{Ca}(\text{NO}_3)_2 \cdot 4\text{H}_2\text{O}$) and diammonium hydrogen phosphate ($(\text{NH}_4)_2\text{HPO}_4$), and NH_3 solution was used to maintain 12 pH [35]. Briefly, Calcium and Phosphorus sources were dissolved in 32.8125 g of calcium source, and 9.5 g of phosphorus source were dissolved magnetically in 200 and 137.5 mL of deionized water at 80 °C, followed by fusion of both solutions by drop-wise addition at 80 °C for 2 h. After 24 h of aging, nHA precipitates were filtered and rinsed with water, followed by drying and calcination at 80 and 500 °C with a vacuum oven and Muffle furnace for 24 and 2 h, respectively.

Synthesis of Whitlockite Nanoparticles (nWH)

Whitlockite was fabricated by the wet chemical precipitation method [33]. For this purpose, 0.13 M $\text{Mg}(\text{OH})_2$ and 0.37 M $\text{Ca}(\text{OH})_2$ solutions were prepared in distilled water. Secondly, equal proportions of $\text{Mg}(\text{OH})_2$ and $\text{Ca}(\text{OH})_2$ were stirred together in distilled water while the temperature was below 100 °C.

Whereas H_3PO_4 0.5 M was added drop wisely with 12.5 mL min^{-1} speed to the above solution. These precipitates

were aged for 24 h to get particles of sufficient size, followed by filtration and calcination.

Preparation of PCL-Cellulose Composite

Four PCL-cellulose composite systems were prepared by solvent casting method, containing (w/w) 100–0%, 95–5%, 90–10%, 85–15% of PCL-MCC respectively. For the first system, 1 g PCL pellets were accurately weighed and evenly dissolved in 20 mL chloroform using a magnetic stirrer at 50 °C for 2 h. Afterward, this homogenous solution was poured into a petri dish and air dried for 24 h to let the solvent evaporate. For PCL/MCC composite preparation, 0.95 g, 0.90 g, 0.85 g of PCL granules and 0.05 g, 0.10 g, and 0.15 g of MCC were dissolved in 15 and 5 mL of chloroform separately by keeping the temperature at 50 °C. Then, both solutions were mixed and stirred for 2 h, followed by air drying.

Preparation of PCL-Cellulose Films with nHA and nWH

Based on the mechanical results of the composites, 95–5% PCL/MCC composite was selected for further analysis. For this purpose, three different composites with three varying amounts (1%, 5%, 10% w/w) of WH and HA were fabricated separately by dissolving 0.01 g, 0.05 g, and 0.10 g of nWH or nHA separately into 5 mL of chloroform. These solutions were mixed with PCL-MCC solution and magnetically stirred for 2 h. Finally, to get the solvent evaporated, solutions were poured into Petri dishes and left air dried for 24 h.

Characterization Techniques

Homogeneity and crystal structure of n HA and nWH Powder were confirmed by performing XRD by DRON8, Russia, with 20 mA current and 40kV voltage. Scherer's formula, $D = k\lambda/\beta\cos(\theta)$, was used to calculate the average crystallite size. Where D represents crystal size, k = shape factor (0.008), λ = incident wavelength, β = broadening of peak at half of the maximum peak, and θ is diffraction angle [36, 37]. WAXD of PCL/Cellulose, PCL/Cellulose/nWH, and PCL/Cellulose/nHA were documented by varying 2θ 5°–90° at the rate of 2° per min at room temperature. Against each measurement, count time per step was 1 s per step, and step size was 0.04.

Vertex 70 FT-IR and Bruker PLATINUM ATR spectrophotometers were used to record FTIR spectra of samples over 500–4000 cm^{-1} set as an observation range. Dried thin films of the PCL/MCC, PCL/MCC/nWH, and PCL/MCC/nHA were placed to get IR data.

Samples were subjected to thermo-gravimetric analysis by carrying out a heating cycle up to 800 °C with a heating rate of 10 °C min^{-1} and a gas flow of 50 mL min^{-1} in each case. The heating range was from 25 to 800 °C under an inert nitrogen atmosphere.

Differential scanning calorimetry (DSC) was performed on DSC 250 under a nitrogen gas atmosphere of 20 mL/min. Each sample of 7 mg was weighed and placed in a Tzero Aluminum pan. Each sample was first heated to 100 °C followed by cooling to – 10 °C and finally heated to 100 °C again. The melting temperature (T_m) and degree of crystallinity (χ_c) were calculated through the following equation as presented in Eq. 1:

$$\chi_c(\%) = \frac{\Delta H_m - \Delta H_c}{\text{wt}\% * \Delta H_m^\circ} \quad (1)$$

Where ΔH_m° is the melting enthalpy of pure PCL whose value is 142 J/g [38] and ΔH_m is the melting enthalpy of samples and ΔH_c is crystallization enthalpy.

SEM analysis was performed on JEOL JSM-6490 A and was utilized to get a morphological assay of the samples. The size and morphology of the nanoparticles were examined by laying sample powder on carbon tape followed by a gold sputter coating of the sample. Cryofracture morphology of virgin polymer, composite, and nanocomposite films was obtained by examining fresh cryofracture surfaces which were produced by dipping films in liquid Nitrogen. And then breaking these samples immediately. Samples were placed on an Aluminum stub, followed by a gold sputter coating. Due to the instability of the polymer at magnification $\geq 10,000\times$, images were not captured at higher magnification.

Tensile properties of the samples were determined under AG-20KNXD Plus (Trapezium-X Universal Testing Machine) with a crosshead speed of 1 mm minute^{-1} . Testing samples were prepared by cutting films with ASTM D6287 (hand cutter) of 20 mm gauge length in 50 × 10 mm (length × width).

Swelling analysis of the nanocomposites was carried out by taking 10 × 10 mm strips of nanocomposites films in a pre-weighed Eppendorf tube. To this, added 1ml of PBS and the Eppendorf tube were placed in an incubator set at 37 °C for 1 month. On days 1, 2, 5, 7, 14, 20 and 24 media were changed and to measure the increase in weight, samples were dried and then placed at a weighing balance. Weight per cent was calculated and resultant data was plotted against time. The swelling ratio of the samples was calculated by the following formula as shown in Eq. 2:

$$S = [(W_s - W_d) / W_d] \times 100 \quad (2)$$

Where W_d and W_s are the weights of the dried and swollen samples respectively.

Biocompatibility Analysis

Cell Culture

Biocompatibility of these composite was assessed by MTT assay, for which Vero cell lines were obtained. Cell lines were passaged on standard conditions 4 times. All sample composite were cut into discs of 15 mm diameter, followed by disinfection with 70% ethanol for 2 h. Prior to carrying out in vitro analysis, samples were further washed with PBS (phosphate buffer solution) and colonized on a sterilized 24-well plate, and compressed. Cell lines were seeded onto the samples with 1×10^4 cells/well strength. Vero cell lines were cultivated in the DMEM medium for 7 days.

MTT Assay

To study the biocompatibility and cytotoxicity of the samples, MTT [(3-(4,5-dimethylthiazol-2-yl)-2,5-diphenyltetrazolium bromide) assay was performed. 100 μL of MTT (5 mg mL^{-1}) which is a cell viability reagent, was first cultivated onto Vero cell lines for 3 h. After incubation, media was removed, and DMSO was transferred onto 96 well plates. Cell viability was calculated by determining UV absorbance by placing the plate on microplate reader at 570 nm. This assay was run in triplicates in three independent experiments [39].

Crystal Violet Staining

Crystal violet staining of the Vero cells on day 7 was carried out. Cells were washed using PBS. After washing, dead cells were removed, and the adhered cells on the bottom of the well were fixed and stained with 0.4% crystal violet solution using methanol for half hour. Cells were again washed to remove excess crystal violet stain and were observed under the microscope. Triplicate images at 200 μm were taken.

LIVE/DEAD Assay

The LIVE/DEAD assay of these composite was assessed using NIH3T3-L1 (fibroblast, adipocyte) cell lines. All sample were cut into discs of 15 mm diameter and sterilized with 70% ethanol for 2 h. Prior to carrying out in vitro analysis, those were further washed with PBS (phosphate buffer solution) and colonized on a sterilized 24-well plate and compressed. Cell lines were seeded onto the samples with 1×10^4 cells/well strength. NIH3T3-L1 lines were cultivated in the DMEM medium for 3, 7, 14, and 21 days. Untreated cells were taken as control, and cells were washed 3 times with PBS, followed by 30-minute incubation with acridine orange ($2 \mu\text{m}$) and Ethidium Homodimer-1 ($4 \mu\text{m}$) ahead of microscopic imaging. To differentiate between live cells (green

color) and dead cells (red color), they were viewed under a fluorescence microscope at wavelengths 494–517 nm and 528–617 nm for Acridine orange and Ethidium Homodimer-1, respectively. Live cells were calculated by Image J software, and field images were captured at $10 \times$.

Animal Testing

All animal experiments were approved by the research committee of the affiliated institution, and all surgical procedures were carried out under aseptic conditions. 12 female mice of age 6–7 weeks were procured. A mouse was divided into four groups. General anesthesia was done by IP injection of 4% chloral hydrate. Prior to making an incision in the thigh muscles, inner thigh hair was shaved and disinfected with iodophor. Afterward, fabricated bone implants having high tensile strength named PC-5, HA-10 and WH-10 were implanted in the thigh muscle. After 2 weeks, mice were sacrificed; dissected muscles were carefully collected and stored in formalin. For further analysis, samples were stained with hematoxylin-eosin and observed under the microscope [3].

Results and Discussion

Structure of the Nanocomposites

Morphology of the Nanoparticles and Nanocomposites Films

nHA and nWH nanoparticles and PCL, PCL/MCC, and PCL/MCC-5 nanocomposites were observed under SEM to visualize their morphology, size, and dispersion of MCC and nanoparticles in PCL-based films. Morphology of nHA [40] and nWH appeared spherical, while the size of HA was 23–40 nm and WH existed in the 17–23 nm range.

Both surface and cryofracture surface images were captured under various magnifications to understand the surface and internal structure of MCC and nanoparticles embedded PCL films, as shown in Fig. 1. Virgin PCL films have smooth and compact structure and have homogeneous features throughout the film as shown in Fig. 1c and d. Upon addition of the MCC in the PCL, we observed homogeneous dispersion of MCC up to 5 wt % and there was no sign of phase separation. MCC rods were observed to have sharp and defined edges. It is vivid from Fig. 1e MCC are embedded in the PCL matrix giving its rough surface topography. As the concentration of MCC was gradually increased in the composites from 5 to 15%, empty spaces were gradually filled, which is attributed to lowering of surface energy which promotes higher cohesion of PCL and MCC [6].

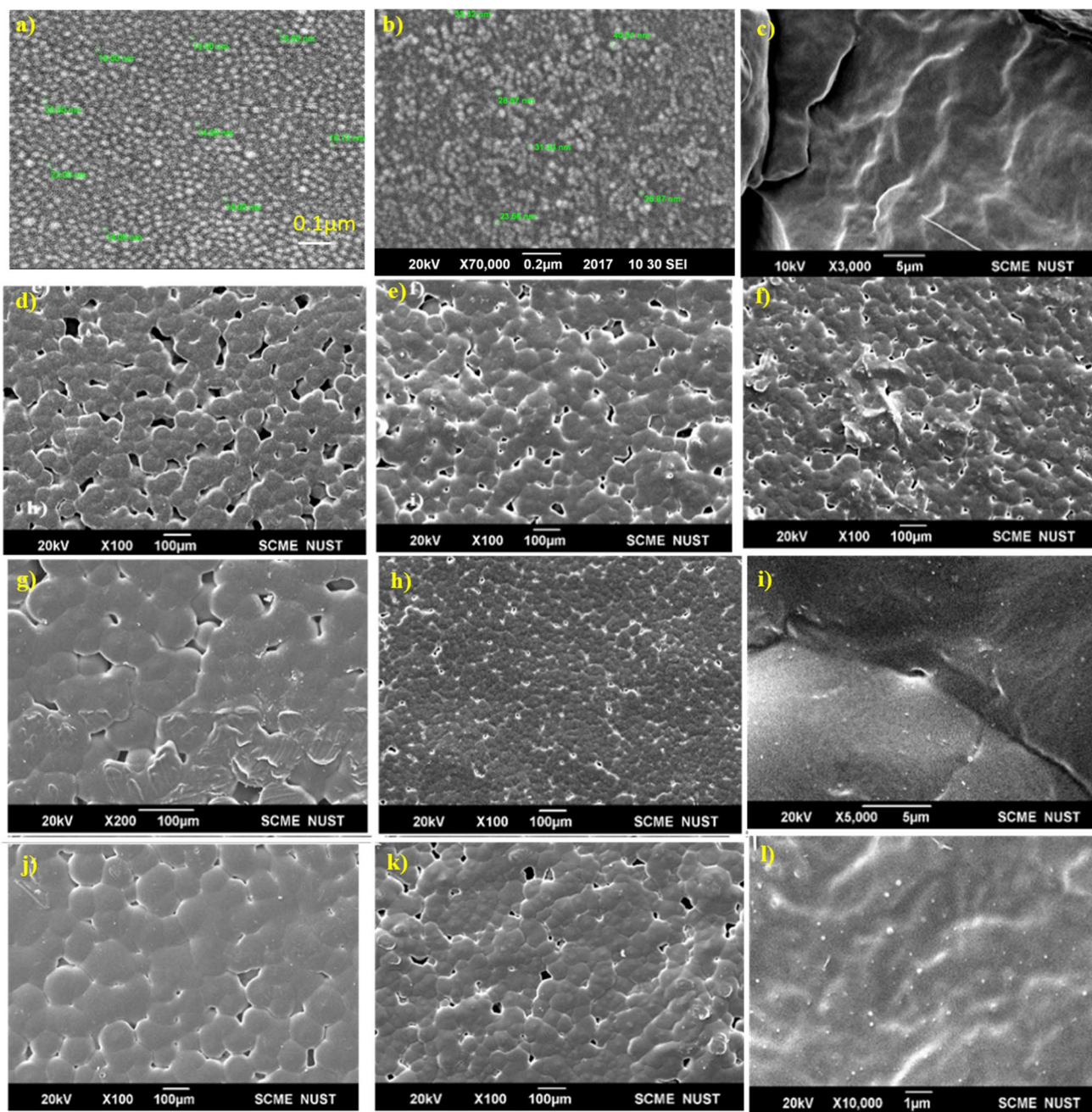


Fig. 1 SEM images of nanoparticles and nanocomposites, **a** nHA Scale bar = 0.1 μm **b** WH, Scale bar = 0.2 μm **c** PCL, Scale bar = 100 μm **d–f** PCL/MCC (5–15%, respectively) Scale bar = 100 μm ,

g–h PCL/MCC-5nHA (1–5%) Scale bar = 100 μm **i** PCL/MCC-5nHA10% Scale bar = 5 μm , **j–k** PCL/MCC-5nWH (1–5%), Scale bar = 100 μm and **l** PCL/MCC-5nWH10% Scale bar = 1 μm

On the introduction of inorganic fillers in the organic matrix, significant changes in the morphology of composites are detected as ceramic nanoparticles are exposed to empty pores surface of the matrix. In the case of PCL/MCC-5/nHA, Fig. 1i–l) shows a homogeneous distribution of nHA in the PCL matrix, while in the case of the PCL/MCC-5/nWH Figure m–p), we observed that some areas of the films have slight agglomerates of the nWH in some

partial locations. Although the incorporation of HA and WH nanoparticles in the polymer matrix significantly influenced the surface topography of the thin films, both nanoparticles further reduced the pore size by filling the empty spaces, which was a consequence of enhanced coherence and extensive networking between filler and base material. Due to the compact and dense structure, the film thickness was reduced to 142.80 and 138.57 μm when HA and WH

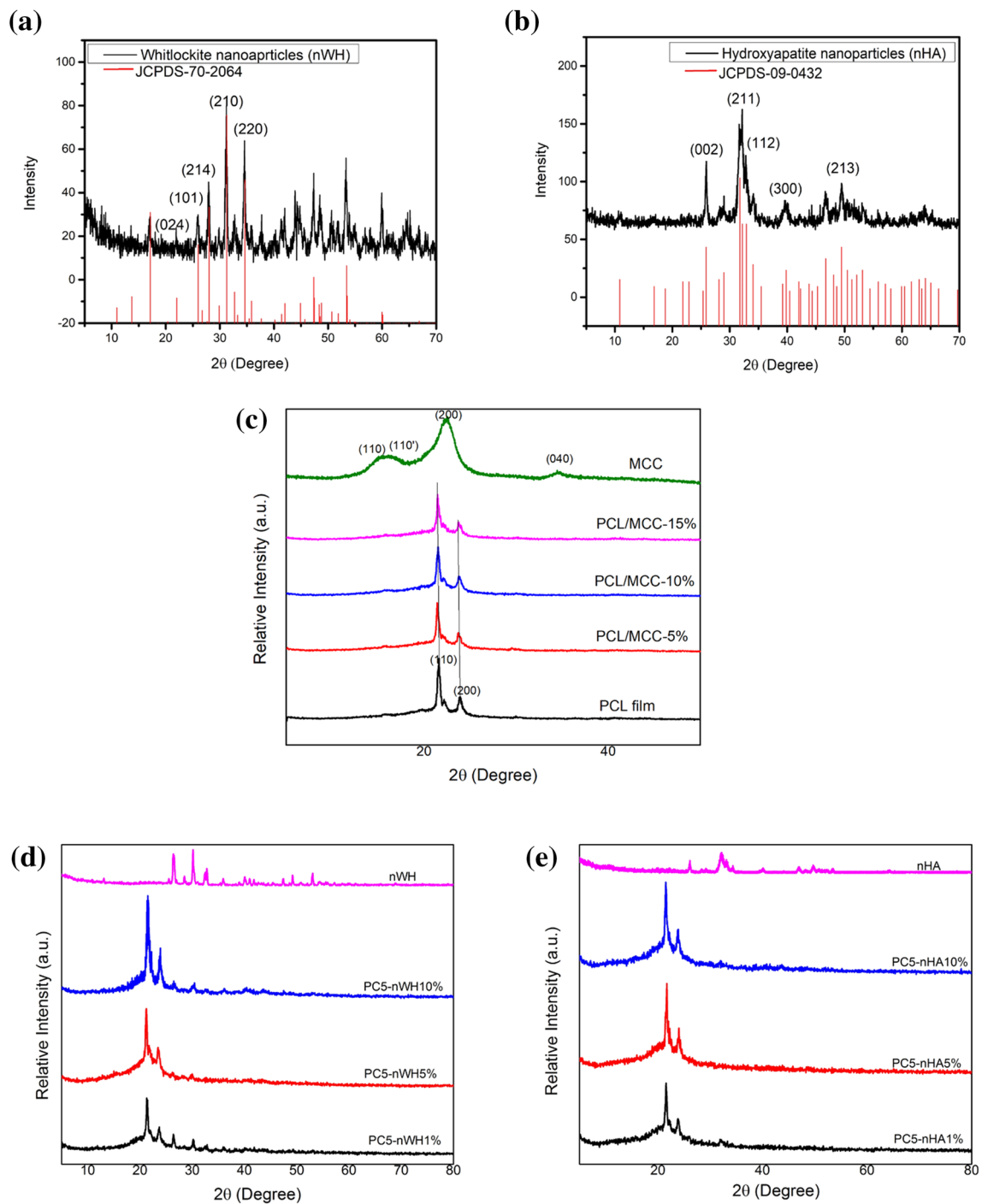


Fig. 2 XRD spectra **a** nWH **b** nHA **c** PCL/MCC composite **d** PC5/nWH nanocomposites **e** PC5/nHA nanocomposites

were added/embedded as filler in 1–10% w/w concentrations, respectively.

X-ray Diffraction Analysis of nHA, nWH Nanoparticles and Nanocomposites Films

Crystallographic analysis of the nanoparticles was done by performing XRD. XRD pattern shown in Fig. 2a has characteristic diffraction peaks of nHA at 2 Theta 25.8°, 31.9°, 32.9, 34.0° and 39.8° corresponded with HA crystal

planes of (211), (002), (300), (310), and (202) matches the JCPDS 09–043 [18, 41]. Crystallite size was calculated to be 22.3 nm. For whitlockite nanoparticles, diffraction peaks are witnessed at two thetas of 44.16°, 37.72°, 34.56°, 32.9°, 31.32°, 28.02°, 25.96° and 17.1° Fig. 2b, representing crystallographic planes (220), (210), (330), (214), (101), and (100) of WH and is according to JCPDS 70-2064 [42]. Crystallite size was found to be 19 nm using Scherer formula.

In Fig. 2c, PCL exhibited two different peaks at 21.5° and 24° at 2θ indicating (110) and (200) crystallographic planes respectively and shoulder peak at 22° [43]. MCC peaks were observed at 14°, 16°, 22.5°, 34° corroborating with the planes (110), (001), (200), and (004), respectively [44]. As MCC is loaded onto PCL, an increase in the peak shoulder of 22.5° is observed, whose peak intensified on increasing MCC loading and a significant change in the crystal structure of the composite is observed. Up to 5% addition of MCC, an increase in the peak intensity is seen, which can be attributed to the nucleation caused by MCC, resulting in an increase in crystallinity of the composites. Addition of MCC in PLLA caused increase in crystallinity because MCC filler acted as a nucleating agent [45]. However, with 10–15% content of MCC, a gradual reduction in the peak intensity and area under the peak is observed, which implies a decrease in the crystallinity as MCC particles start to cluster [20].

After the addition of nHA 1%, 5% and 10% in the PCL-MCC blend of 95–5% w/w concentration, respectively, it was observed that PCL peaks at $2\theta = 22^\circ$ and 24° remained intact. An additional peak at $2\theta = 31.8^\circ$ appeared, corresponding to (211) planes of the apatite particles as shown in Fig. 2e. At 10% addition of nHA particles, a small peak at 26.05°, which tallies with the (002) reflective planes of nHA, is also observed. For the nWH addition in the PCL-MCC composite, as shown in Fig. 2d, peaks for nWH are observed at 26.5°, 28.6°, 30.3°, and 32.9°, which matches with the (214), (300), (0210) and nWH (220) crystal planes, in addition to PCL peaks at 22° and 24°. As the amount of nWH and nHA nanoparticles is increased from 1 to 10% w/w, a gradual increase in the intensity of the peaks is observed, which implies that these particles act as nucleating agents, causing improved alignment, closer packing, and orientation for the PCL/MCC films which further results in the improved crystallinity of the matrices.

FTIR Analysis of the Nanoparticles and Nano Composite Films

FTIR was carried out to check interaction between inorganic filler and organic polymer matrix in nanocomposites. No chemical degradation of the any constituent materials is indicated in FTIR spectra. FTIR is used to identify functional group present in the nanocomposites as well as

to analyze the chemical change between nanocomposites after mixing. The synthesized nHA compound was subjected to FTIR. The presence of peaks at 1092 (PO_4^{3-} , ν_1), 1023 (PO_4^{3-} , ν_1), 963 (OH^{-1}), 601 (HPO_4^{2-}), and 561 cm^{-1} (PO_4^{3-} , ν_3) were the reported characteristic bands of nHA [30, 46, 47]. A small peak at 3571 cm^{-1} is assigned to OH. It is interesting that the amount of H_2O is minute as shown in Fig. 3b. A distinguishable band at 963 cm^{-1} was observed and attributed to asymmetric P–O stretching vibration of PO_4^{3-} . Additionally, a mild sharp band seen at 631 cm^{-1} corresponded to deformation mode of O–H. For nWH, FTIR bands are shown in Fig. 3a and were witnessed at 582 and 571 cm^{-1} , double peak (ν_4 , bending of PO_4^{3-}), 989 cm^{-1} (ν_1 , P–O–H stretching of HPO_4^{2-}), 884 cm^{-1} (ν_3 , HPO_4^{2-} bending), and 1059 cm^{-1} (ν_3 of PO_4^{3-}) bending [31–33]. A comparatively sharp peak at 1346 cm^{-1} correspond to P(O–H) [34] while, two bands at 2794 and 2374 cm^{-1} are allotted to P–O overtone on the previous data basis [32].

FTIR of virgin MCC as shown in Fig. 3c. showed a broad peak at 3333 cm^{-1} and a small peak at 1636 cm^{-1} due to stretching of hydrogen bonded OH groups on the surface. A band at 2905 cm^{-1} corresponded to the asymmetric bending of C–H functional group. Owing to the C–O group vibration, a strong absorption band was observed at 1050 cm^{-1} [48].

FTIR analysis of both virgin PCL and PCL film were performed and spectra with characteristic peaks were obtained. Peaks at 2943 cm^{-1} , 2865 cm^{-1} , 1720 cm^{-1} , 1240 cm^{-1} (crystalline phase of PCL), 1159 cm^{-1} (amorphous phase of PCL), attributed to the asymmetric stretching of CH_2 , symmetric CH_2 ν_s stretching, C=O bending of ester group, COC asymmetric bending, and symmetric stretching of C–O–C respectively, were characteristic bands of PCL. A sturdier intensity band corroborated with XRD data, corresponds to the amorphous phase [49].

On addition of MCC to PCL, typical peak of cellulose disappeared due to dehydration and the expected reaction between carbonyl group of PCL and hydroxyl group of MCC did not occur which lead to non-displacement in the carbonyl peak. But the peak areas of CH_2 and C–O–C groups reduced on the cellulose loading, which suggested the augmentation in the crystallinity of PCL on the gradual loading of MCC [48].

Upon the addition of HA in 1%, 5%, and 10% wt/wt percentage as shown in Fig. 3e, characteristic PCL bands are observed at 2943 cm^{-1} , 2865 cm^{-1} and 1720 cm^{-1} , along with characteristic PO_3^{-4} peaks at 561 cm^{-1} while the peak at 1023 cm^{-1} is shifted towards greater wavenumber 1044 cm^{-1} , and 1092 cm^{-1} is shifted shifted at 1110 cm^{-1} . New bands at 1591 cm^{-1} , 1503 cm^{-1} and 821 cm^{-1} appear confirming the vander waal interaction interaction between PCL and nHA. The overall intensity of the PCL bands is reduced upon the incorporation of nHA.

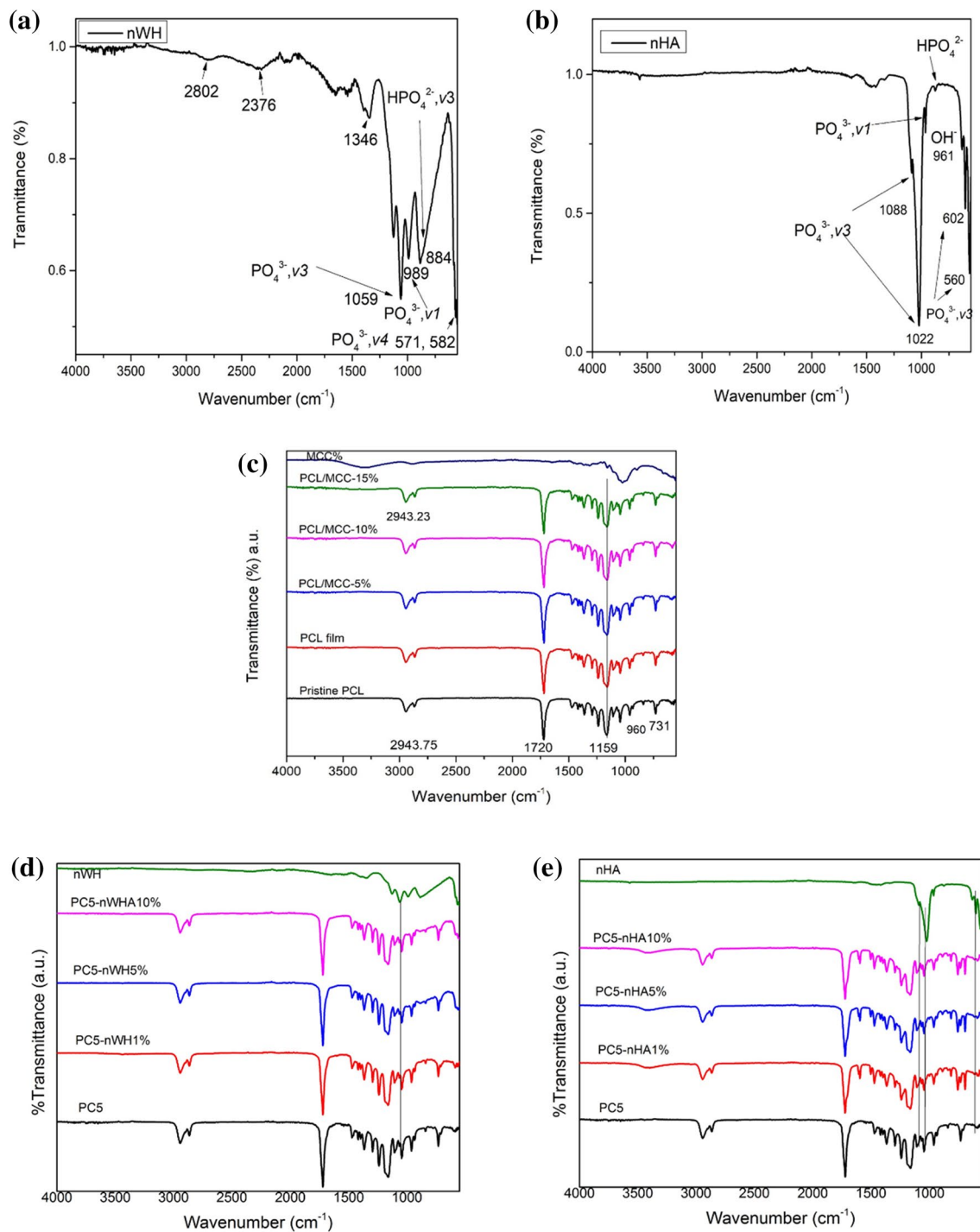


Fig. 3 FTIR spectra **a** nWH **b** nHA **c** PCL/MCC composite **d** PCL/MCC-5nWH nanocomposites **e** PCL/MCC-5nHA nanocomposites

On the incorporation of nWH in PCL as shown in Fig. 3d, characteristic PCL vibrational bands are intact with slight reduction in their intensity. Characteristic WH bands at 989 and 884 cm^{-1} are not apparent when

WH concentration is 1% but when its content is increased to 5–10% it becomes prominent and shifts towards lower wavenumber, while one at 1067 cm^{-1} is merged in the PCL bands.

Thermo-Mechanical Properties of the Nanocomposites

Thermo-Gravimetric Analysis (TGA)/Differential Thermal Analysis (DTA)

To check the thermal stability of the nanocomposites and change in weight%, TGA was conducted by heating at constant rate. TGA is also helpful in determining the maximum temperature that scaffolds can bear in thermal processing and their homogeneity. Thermograms from TGA/DTA of PCL/MCC composite and nanocomposites are shown in Fig. 4a, b, and c. Table 1 enlists DTA and TGA peaks measurements. Virgin PCL shows thermal degradation in one step at 313 °C which is consistent with the previously reported in literature [50] with 89.1% mass loss. However, incorporation of cellulose caused a significant increase in the degradation temperature of PCL. These composites showed two step thermal degradation depending upon the weight percentages of PCL and MCC. In case of nanocomposites, final residues were found at 322–326 °C proving that composites have completely degraded. Here, the weight loss was similar to the MCC and HA/WH concentrations.

In addition, an upsurge in the thermal stability is observed for 5%, 10% and 15% incorporation of MCC in PCL with mass loss of 92.8%, 91.31%, and 93.7%, respectively. Maximum thermal stability is observed when MCC concentration is 5% w/w, and 10%, while for 15% a gradual decrease is observed but still better than PCL alone. The melting point of PCL increased on the incorporation of MCC. This increased thermal stability can be attributed to the positive interactions between MCC and PCL. Due to hydrogen bond formation between carbonyl groups of PCL and hydroxyl groups of MCC, dehydration of MCC is delayed, char and gasses formed by the degradation of cellulose react with the solid PCL causing improved thermal stability. So MCC acts as stabilizer which explains increment in the thermal

stability [51]. With the increment of nHA and nWH in PCL/MCC-5 matrix, onset temperature of thermal decomposition and maximum degradation temperature are enhanced thus establishing that nHA and nWH act as reinforcing agent. Khanmohammadi .S reported increase in thermal stability when PCL was composited with MCC and nanocomposited with ZrO₂ [52].

The inclusion of nHA and nWH showed a significant variation in the stability of the product. In case of nanocomposites, mass loss up to 200 °C is due to removal of absorbed water and lattice water while mass loss up to 456 °C is attributed to the decomposition of hydrogen phosphate ions to pyrophosphate ions [53]. By comparing the relative thermal stabilities of the nanocomposites, it is concluded that incorporation of nHA and nWH improves their thermal stability.

Differential Scanning Calorimetry (DSC)

DSC of the polymeric nanocomposites is conducted to better understand their crystallinity and structure. DSC thermograms of virgin PCL, MCC, PCL/MCC composite, and nanocomposites for the first heating scan, cooling scan and second heating scan are presented in Fig. 5a–f. T_m , T_c , and degree of crystallinity X_c (%) values of PCL/MCC composite are presented in Table 1.

In general, melting temperature values (T_m °C) and crystallization temperature (T_c °C) values of PCL-MCC composite Fig. 5a, b suffered minor shift in values as compared to the of virgin PCL. In the heating curve, Fig. 5a T_m value have for virgin PCL was 56 °C which remained almost same after 5, 10, and 15 wt % addition of MCC. T_c values were obtained from crystallization curve thermograms as shown in Fig. 5b lowered from 30.74 °C for virgin PCL to 28.91 °C for 5 wt% MCC, then increased to 29.41 °C for 10 wt% MCC and 30.17 °C for 15 wt% MCC. Coca .M et al. studied PCL/cellulose bio composite and reported increase in crystallinity as compare to PCL [54]. Mi et al. and Celebi et al.

Table 1 Thermal analysis (TGA and DTA) of PCL composites and nanocomposites

Polymer system	Sample code	TGA curve temp. (°C)		DTA curve temp. (°C)		Loading of nHA(g) / nWH
PCL	PC	373	–	417	447	–
PCL/MCC-5%	PC5	395	461	399	465	–
PCL/MCC-10%	PC10	390	447	406	451	–
PCL/MCC-15%	PC15	383	439	390	435	–
PCL/MCC-5%-nHA1%	PC5-HA1	416	460	416	470	0.01
PCL/MCC-5%-nHA5	PC5-HA5	393	451	399	456	0.05
PCL/MCC-5%-nHA10%	PC5-HA10	395	449	386	458	0.10
PCL/MCC-5%-nWH1%	PC5-WH1	407	–	426	–	0.01
PCL/MCC-5%-nWH5%	PC5-WH5	392	458	401	456	0.05
PCL/MCC-5%-nWH10%	PC5-WH10	385	447	400	425	0.10

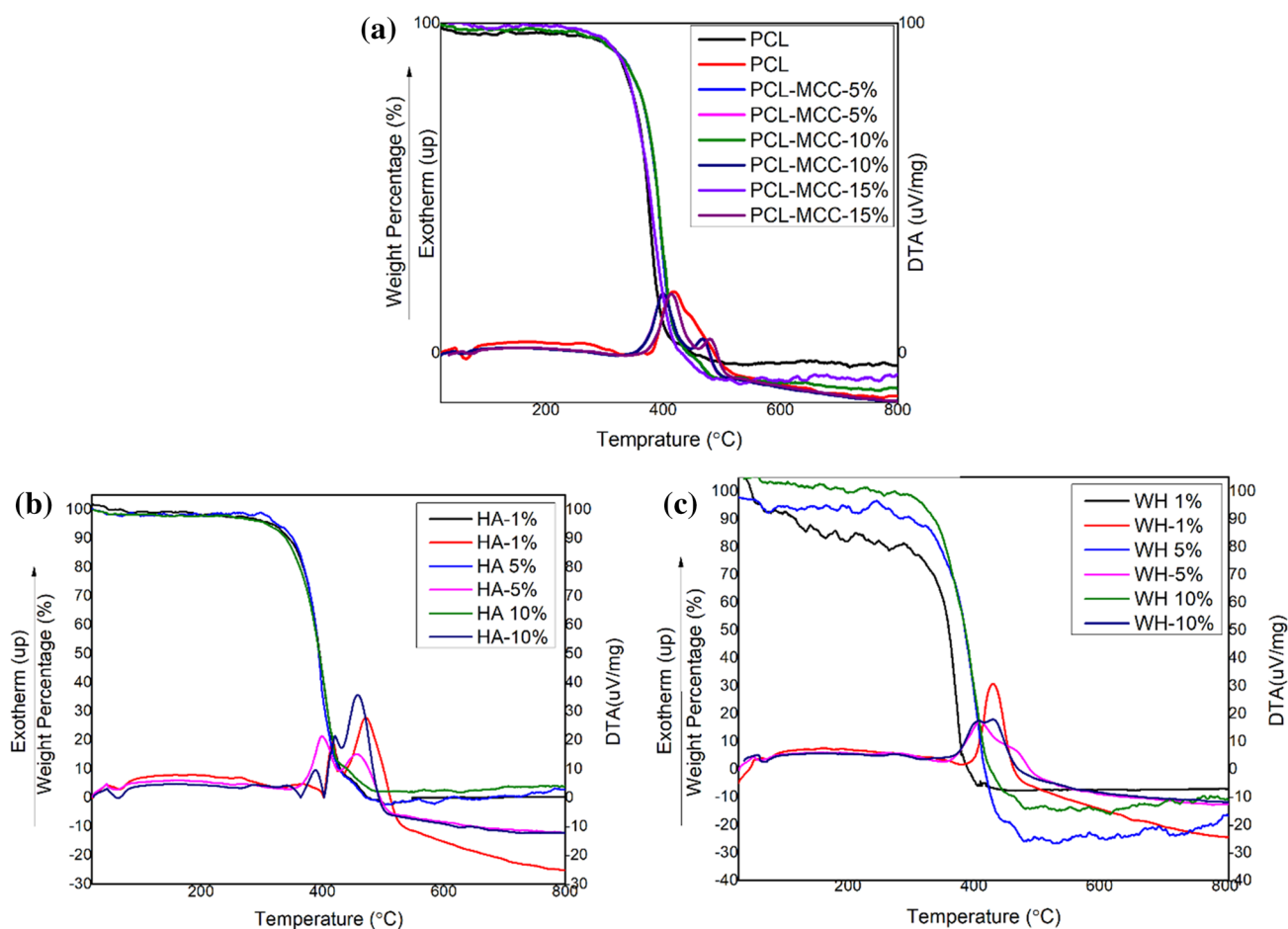


Fig. 4 TGA and DTA of **a** PCL/MCC, **b** PCL/MCC-5/nHA, and **c** PCL/MCC-5/nWH, where HA (1–10%) and WH (1–10%) represents 1–10 wt% of nanoparticles in the PCL/MCC-5 composite

reported induced crystallization of cellulose caused increase in crystallinity and decrease in PCL chain mobility [55, 56]. Similar behavior was observed in our composites (Table 2).

In case of nanocomposites Fig. 5c, d, T_m values show consistent increase with increasing nanoparticle concentration. T_m values obtained from heating curve improved from 58.02 °C to 1 wt% HA to 58.20 °C for 5 wt% HA, and 58.34 °C for 10 wt% HA. With the incorporation of whitlockite, T_m values augmented from 57.51 °C to 1 wt% WH to 58.17 °C for 5 wt%, and 58.31 °C for 10% WH. Change in the thermal behavior was small as compared to the virgin PCL it still.

The degree of crystallinity showed an ascending trend on the inclusion of filler and nanoparticles, as a gradual increase in the crystallinity was observed while, maximum crystallinity was witnessed with HA-10 and WH-10. The X_c value increased from 19% for PCL/MCC-5 to 19.7% for 10 wt% HA, and 20.1% for 10 wt% WH. The calorimetric findings are consistent with XRD and FTIR analysis of polymer composite and can be attributed to the reinforcement and

nucleation effect of the nanoparticles. When concentration of the MCC particles reaches up to 10–15%, due to lack of interaction with matrix and availability of low interfacial area hinders it to act as nucleating agent and consequently prevents increment in crystallinity. It is widely accepted

Table 2 Representing the T_m , T_c , and degree of crystallinity X_c (%) values of PCL/MCC blend

Sample code	T_c (°C)	T_{m2} (°C)	X_c (%)
PF	30.74	56	17
PCL/MCC-5	28.91	55.58	19
PCL/MCC-10	29.41	55.50	18.5
PCL/MCC-15	30.17	55.48	18
PC5/nHA1%	–	58.02	19.2
PC5/nHA5%	–	58.20	19.5
PC5/nHA10%	–	58.34	19.7
PC5/nWH1%	–	57.51	19.4
PC5/nWH5%	–	58.17	19.8
PC5/nWH10%	–	58.31	20.1

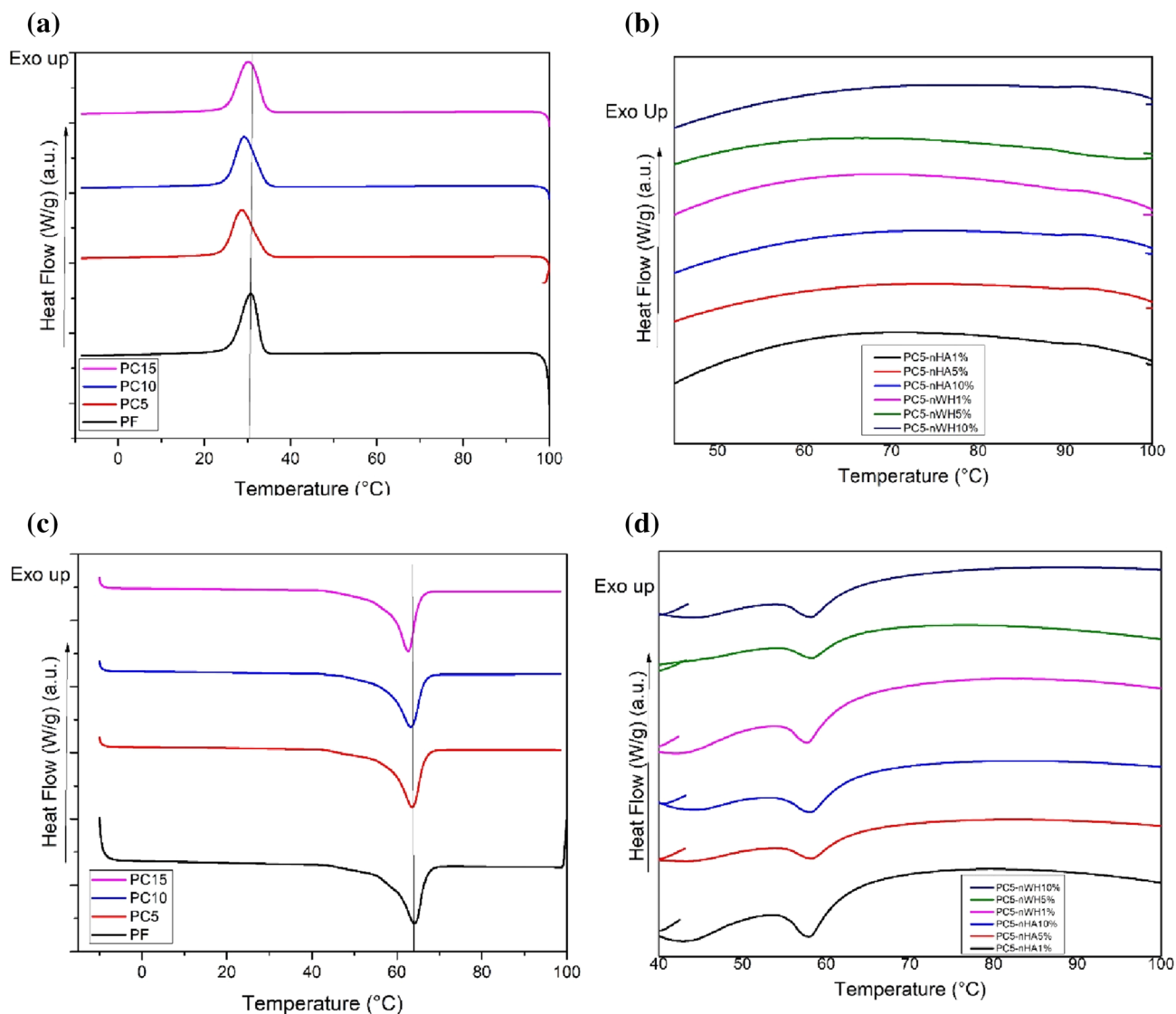


Fig. 5 DSC analysis at the heating rate of 10 °C/min: **a** second heating curve of PCL/MCC composite, **b** cooling curve of PCL/MCC composite **c** second heating curve PC5/nHA and PC5/nWH, and **d** cooling curve of PC5/nHA and PC5/nWH

that the crystalline cellulose acts as a nucleating agent for biopolymers [45, 57].

Mechanical Properties

Figure 6a, d, e, f, shows stress-strain curves obtained from tensile mechanical testing of PCL, PCL/MCC composite with different loadings of MCC (5%, 10%, and 15%) wt./wt. concentration. PCL is a rigid polymer having high tensile strength but breaks at the elongation value of 355% strain. From these curves, it can be interpreted that when 5% concentration of MCC was added to the PCL, a substantial increase in the ultimate tensile strength, elongation at break point and Young's Modulus was observed, which contrasts with when 10% and 15% of MCC was added.

Tensile mechanical properties are dependent on the matrix and filler weight%. The tensile modulus of PCL/MCC-5 is increased by ~ 106% from 888.27 ± 1.21 to 938 ± 1.45 MPa, elongation at break point also increased by ~ 152% from 355.29 to 541.63. When 10% MCC is added ultimate tensile strength values decreased by ~ 67% from 6.56 to 4.45 MPa and Modulus was reduced by ~ 92% from 888.27 ± 1.21 to 824 ± 2.0 while, the elongation at break point increased by 122% than pure PCL. Similarly, when 15% MCC was added in the pure PCL system Young's Modulus lowered by ~ 96% from 888.27 ± 1.21 MPa to 852 ± 0.05 MPa, strain % reduced by ~ 49% from 355.29 to 173.9 and UTS values drastically reduced by ~153% from 6.56 to 4.27 MPa. This implies that addition of MCC in PCL is showing saturation in effect and thus, tensile Modulus and ultimate tensile

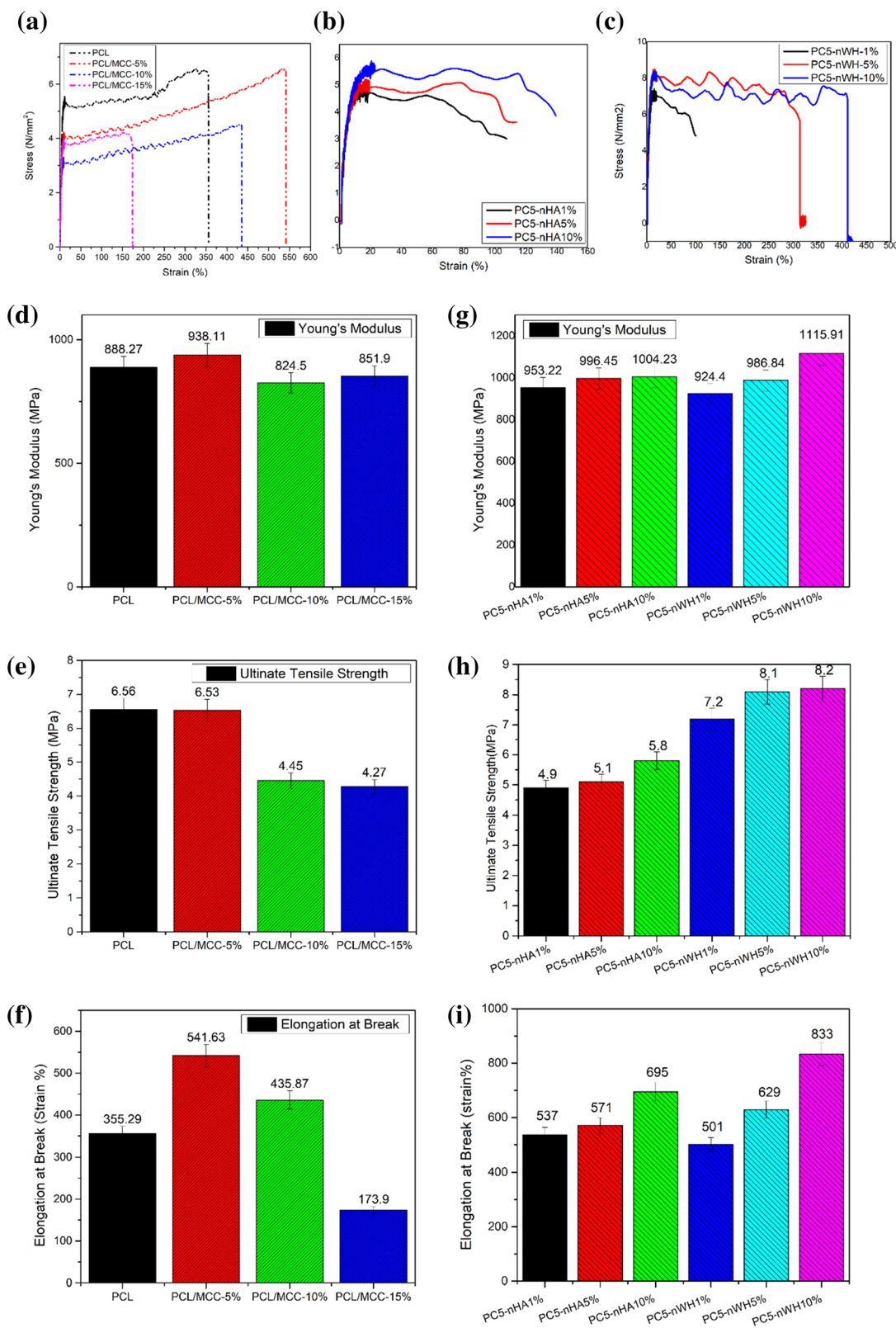


Fig. 6 Mechanical properties: Stress strain curves **a** PCL/MCC, **b** PCL/MCC-5/nWH, and **c** PCL/MCC-5/nHA. Young's modulus **d** PCL/MCC, **g** PCL/MCC-5/nWH, and PCL/MCC-5/nHA. Ultimate

tensile strength **e** PCL/MCC and **h** PCL/MCC-5/nWH, PCL/MCC-5/nHA. Elongation at break **f** PCL/MCC, **i** PCL/MCC-5/nWH, and PCL/MCC-5/nHA

strength are decreasing but still we have better elongation at break as compared to PCL. Upon reaching 15% MCC concentration, mechanical properties decreased drastically. This decrease in the mechanical properties can be attributed to the decrease in the nucleation effect and increase in crystallinity. When filler concentration exceeds limit value (10%), particles start to agglomerate owing to the lack of interaction with the matrix which lead to decrease in the interfacial area acting as point of nucleation thus, causing brittleness [45]. These agglomerates not only weaken the composite material but also impedes layer to layer adhesion.

When HA and WH were incorporated into composite films in 1%, 5%, and 10% w/w percentage, a substantial increase in all mechanical characteristics was witnessed. Figure 6b, c, g, h, and i shows the stress-strain curve of tensile testing of HA1, HA5, HA10, WH1, WH5, and WH10 respectively and compared with the virgin PCL and PCL/MCC-5. For 1%, 5%, 10% addition of HA, modulus increased from 938 MPa to 954.25 MPa, 996 MPa, and 1004.26 MPa respectively and elongation at break augmented from 435.87 to 537%, 571%, 695%, while the UTS values decreased 6.35 MPa from to 4.9 MPa, 5.1 MPa, and 5.8 MPa. When WH was inserted in same fraction as of HA, strain percent value enhanced from 435 to 501%, 629% and 833% and UTS amplified from 6.35 MPa to 7.2 MPa, 8.1 MPa, and 8.2 MPa, while tensile Modulus values enlarged from 938 MPa to 923.25 MPa, 980.45 MPa and 1115.91 MPa. This lowering in the UTS values is due to agglomeration of nHA and nWH particles in the polymer matrix which is owing to absence of hydrogen bonding between filler and polymer matrix. It is observed that nanoparticles distribution is homogenous and random in nanocomposites. While, an incessant increase in the tensile strength is attributed to the synergistic effect of filler and matrix as filler inhabits pores of matrix and load is shifted to the filler and it acts as reinforcing agent [58]. The bonding of the nanoparticles with the polymer matrix can lead to retardation, interruption and even blockage of the micro crack formation and propagation. The intimate interaction between polymer matrix and nanoparticles results in enlargement of matrix's local stress which is then transferred to the nanoparticles. Hence, inclusion of nanoparticles can delay or interrupt the expansion and growth of cracks by stress distribution. Furthermore, these inorganic fillers also enhanced density and crystallization of the polymer which is useful for improving hardness of the composites [3]. Cancellous bone requires the elastic modulus of 0.1–4.5GPa, whereas 17 GPa of cortical bone [59]. Based on these values, it is established that above mentioned films are a good contender for the cancellous bone substitute. It can be assessed from the results that by changing the nanoparticle concentration in the nanocomposites, mechanical properties of the polymers can be fine-tuned.

Nanocomposites as a Biomimetic Scaffold

Swelling Analysis

Swelling properties of the virgin PCL, PCL-MCC composite and nanocomposites of PCL-MCC with nHA and nWH were studied until equilibrium was achieved. Swelling analysis helps to understand surface, mass transfer properties and solvent diffusion as it depends on the network density and polymer structure. During the assessment of scaffolds for their application in tissue engineering, swelling behavior is an important index because inadequate solvent absorption hinders cell growth and excessive absorption leads to destruction of scaffold's morphology [60]. Swelling behavior of the virgin polymers, composite and nanocomposites is shown in Fig. 7. The virgin PCL shows high dimensional stability than PCL-MCC composite due to its semi-crystalline and hydrophobic nature which implies that in the semi distorted arrangement of PCL chains no sufficient spaces are present to accommodate solvent molecules. While, with the addition of MCC an increasing trend in the swelling behavior is observed which can be attributed to the OH groups present on the MCC surface [61].

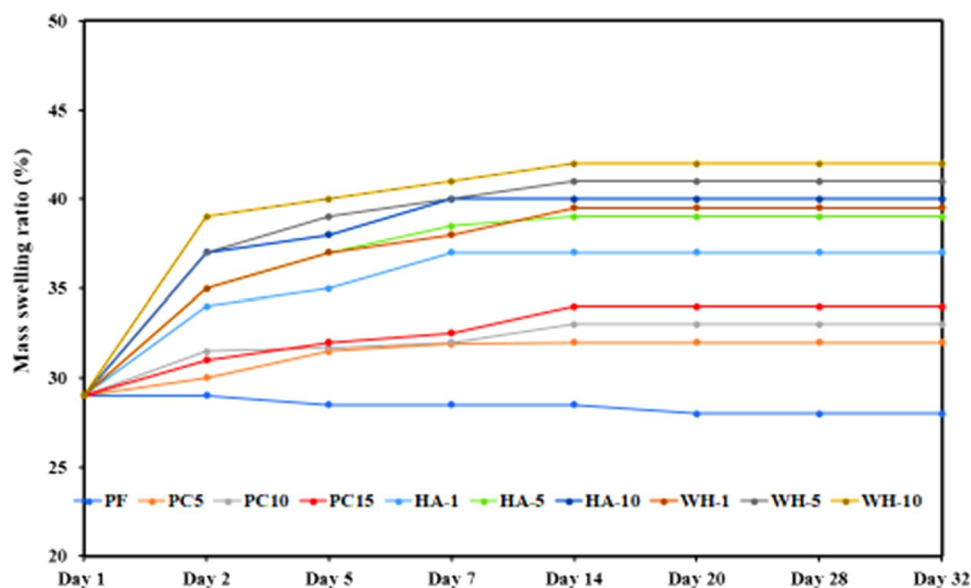
Addition of nHA and nWH up to 10% in the composite lead to further escalation in swelling ratio and improved nanocomposites' fidelity. This indicated that nanoparticles anchor polymeric chains firmly in their neighborhood, eventually leading towards enhanced network density. This cross-linked networking and hydrophilic moieties not only enhances integrity of the nanocomposites, but also is a prime factor in growth of swelling ratio [62]. A dramatic change is observed in first 24 h and after that equilibrium is achieved.

Cell Culture

We designed PCL/MCC composite decorated with nWH and nHA for bone regeneration scaffold. To introduce any material as a scaffold in tissue engineering, it's important to study its cytocompatibility profile. Cytocompatibility profile is assessed through cell adhesion, proliferation and viability studies [9]. Cell adhesion facilitates the interaction and binding of cells with extra cellular matrix. However, cell proliferation is associated with cell growth resultant of cell division [36]. Cell viability is the ratio of many live cells to the whole population of cells. It is expressed in percentages. Herein, two cell lines, namely Vero and NIH3T3-L1, were cultured on hybrid scaffolds' surface to report cell viability by MTT, crystal violet staining, and Live/Dead fluorescence assay.

Vero cell lines were cultured on the surface of PCL, PCL-MCC composite and PCL/MCC nanocomposites with nHA and nWH to understand the cell adhesion and viability studies, as shown in Fig. 8a. From the cell

Fig. 7 Mass swelling behavior of PCL/MCC composite, PCL/MCC-5 nanocomposites with respect to time



viability data, the virgin nanoparticles have cell viability of ~70.66% and ~72.30% for nHA and nWH, while virgin PCL has ~86.56%. These nanoparticles were composited with PCL/MCC-5; the cell viability of the resulting nanocomposites is higher than the virgin nanoparticles. In case of PCL/MCC composite with the highest cell viability are shown by PCL/MCC-5, which is around 87.75%. On further addition of MCC in PCL at 10 and 15 wt%, cell viability decreased from virgin PCL. However, adding nWH and nHA in PCL/MCC-5 increased the cell viability on the scaffold surface. In the case of the PCL/MCC-5/nWH, adding the nanoparticles amplified cell viability compared to virgin PCL and PCL/MCC-5. In conclusion, all the HA nanocomposites showed more than 90% cell viability. From these cytocompatibility results, it may be assessed that there was no compromise on biocompatibility according to standard ISO 10993-5:2009 [63]. The introduction of the nanoparticles and MCC in PCL caused an increase in the hydrophilicity of the scaffold resulting in increased cellular viability on the scaffold surface.

Cellular morphology and adhesion in the surface of the films were studied by taking the phase contrast images after staining the cells with crystal violet, as shown in Fig. 8b. Cells showed branched and interconnected networks with morphology suggesting successful cell adhesion and proliferation on the surface of the scaffold. In the case of the nanocomposites, the cell population on the surface of the scaffold increased, demonstrating that nanoparticles provided cell anchoring sites which magnified cellular function [64]. From the PCL/MCC-5/nWH, it is clear that cells are well anchored on the scaffold surface, further corroborating the cell viability results.

Samples were subjected to Live/Dead assay by culturing NIH3T3-L1 cell lines on the surface of polymer composite and nanocomposites for 3, 7, 14 and 21 days using acridine orange/ethidium bromide dual fluorescent staining. Figures 9 and 10 represent that live cells' cytoplasm is stained green, and those of dead cells are stained red. On day 3, seeded cells started to adhere to the nanocomposite surface. Scaffolds containing cellulose and nanoparticles showed improved adhesion because virgin polymer surface is hydrophobic, while the incorporation of filler and nanoparticles provided additional attachment sites by amplifying hydrophilic character. On day 7, the proliferation of attached cells is witnessed owing to good morphology, cell division and interconnected network. From day 3 to day 7, a 10–20-fold increase in the proliferation rate is evident as concentration increases from 1 to 10%. On day 14, a branched and interconnected cellular network is formed by migrating, elongation and aggregating cell metabolites. While on day 21, cell death is observed in polymer composite and hybrid scaffolds due to apoptosis-associated changes. In comparison to the nWH-based hybrid scaffold, nHA-based scaffolds showed better cell adhesion and proliferation morphology for days 3, 7 and 14. While on day 21, WH at 10% in PCL/MCC-5 nanocomposites have maximum cell population on their surface [59, 65, 66].

Bio Interfacial Affinity and Biocompatibility of Nanocomposites

To assess biocompatibility, bio-interfacial affinity and anti-inflammatory activity of the nanocomposites, samples with high mechanical strength were embedded in the thigh muscle

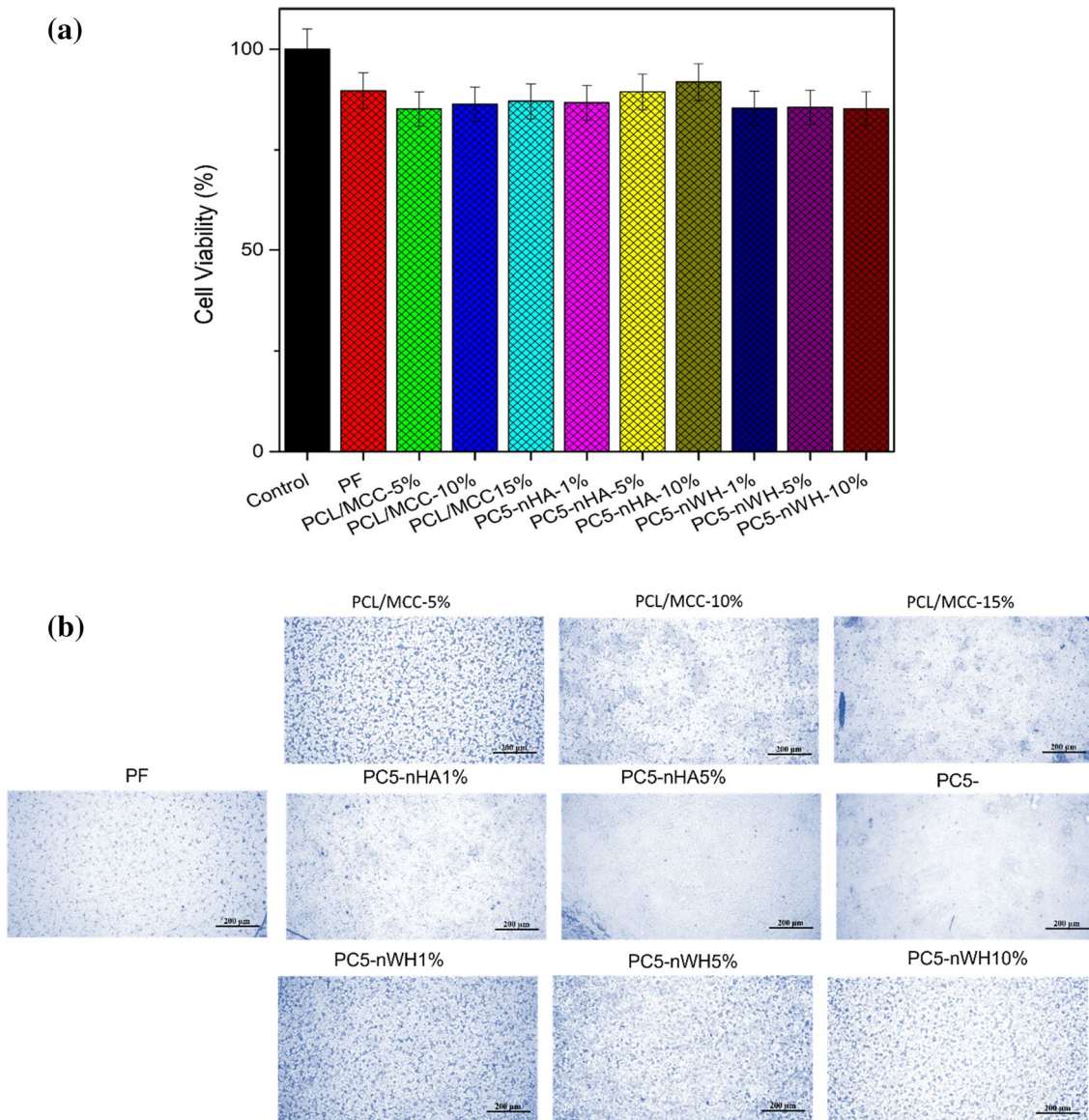


Fig. 8 **a** Cell viability calculation of nanocomposites after 7 days of cell culture. Data is statistically significant ($p \leq 0.05$). **b** Cell adhesion images of the nanocomposites stained with crystal violet on day 7. Scale bar is 200 μm

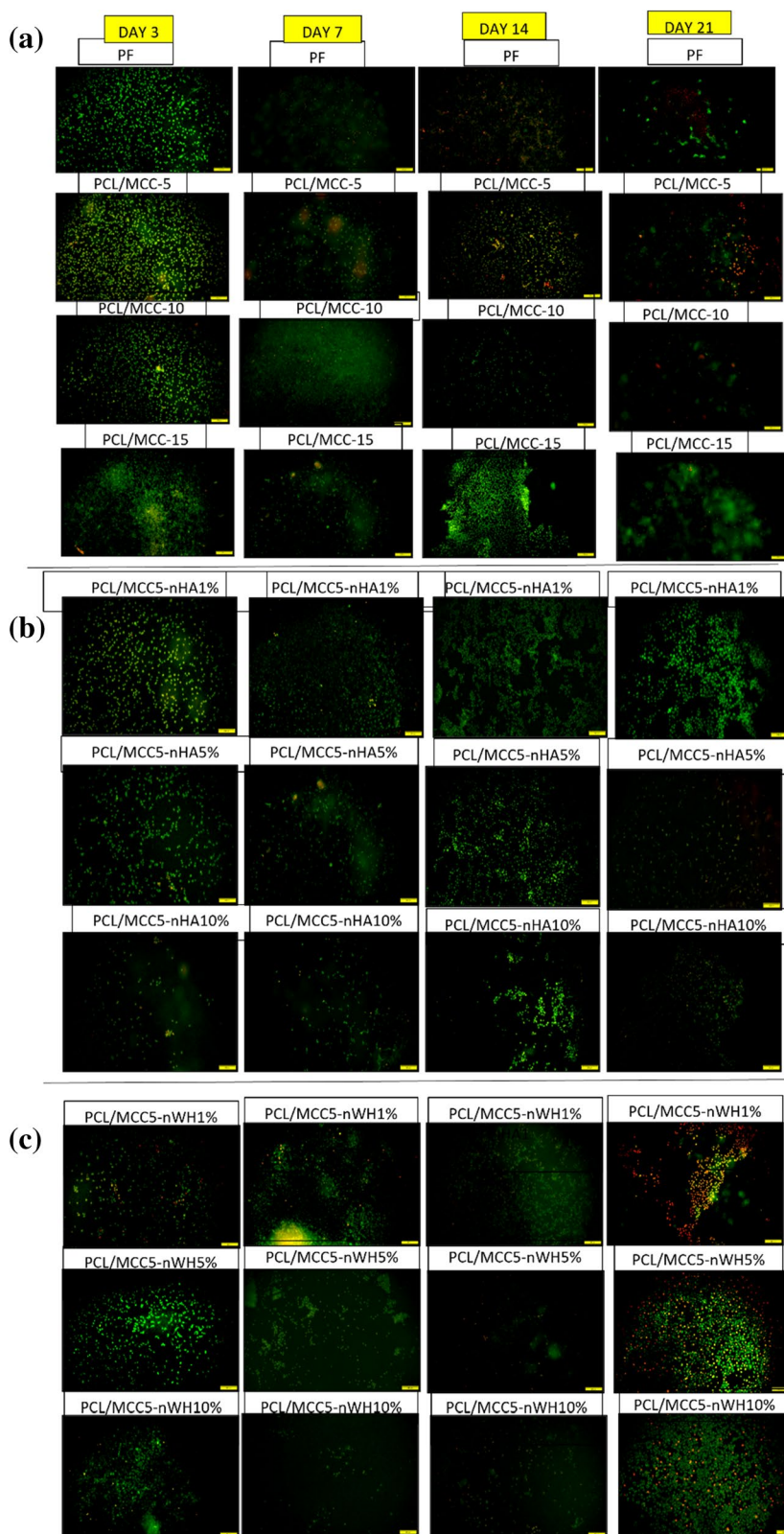
of the female mice for 2 weeks [67]. It can be seen in Fig. 11. A very small muscle adhered to the surface of PCL/MCC-5 and during implant was easily drawn out, which implies that PCL/MCC-5 had little or no bio-interfacial affinity. In contrast, nHA-10 and nWH-10 nanocomposites showed concentrated and thick muscle adherence and significantly higher bio-interfacial affinity. It is worth mentioning that HA-10 displayed enhanced inter-facial bonding compared to nWH-10 by promoting encapsulation and adhesion of muscle. This can be attributed to the continued release of Mg^{2+} ions, which plays a role in enzyme-catalyzed cellular reactions by modulating transcription factors. Histological studies show that PCL/MCC-5 has numerous inflammatory

cells while incorporating WH and HA suppressed inflammatory reactions.

Conclusion

PCL/MCC composites were prepared by varying 5, 10, and 15 wt% MCC in PCL matrix to obtain mechanically optimized PCL/MCC-5 composite. Novel biomimetic nanocomposites of PCL/MCC-5 embedded with 1, 5, and 10 wt% loadings of nHA and nWH were prepared for enhanced bone repair and regeneration applications. PCL/MCC and PCL/MCC composites with nHA and nWH were evaluated on

Fig. 9 Live Dead Assay of NIH3t3-L1 cell lines for day 3, 7, 14, and 21. **a** PCL/MCC composite, **b** PCL/MCC-5-nHA composites **c** PCL/MCC-5-nWH composites, Scale bar is 100 μm



crystal structure, thermo-mechanical, morphological, degradation, and biological properties. SEM images showed that MCC has decreased pore size of PCL film with increasing

MCC content, while nanoparticles are homogeneously dispersed in the PCL/MCC-5 matrix up to 5 wt% and above that agglomeration occurred. FTIR spectroscopy, XRD

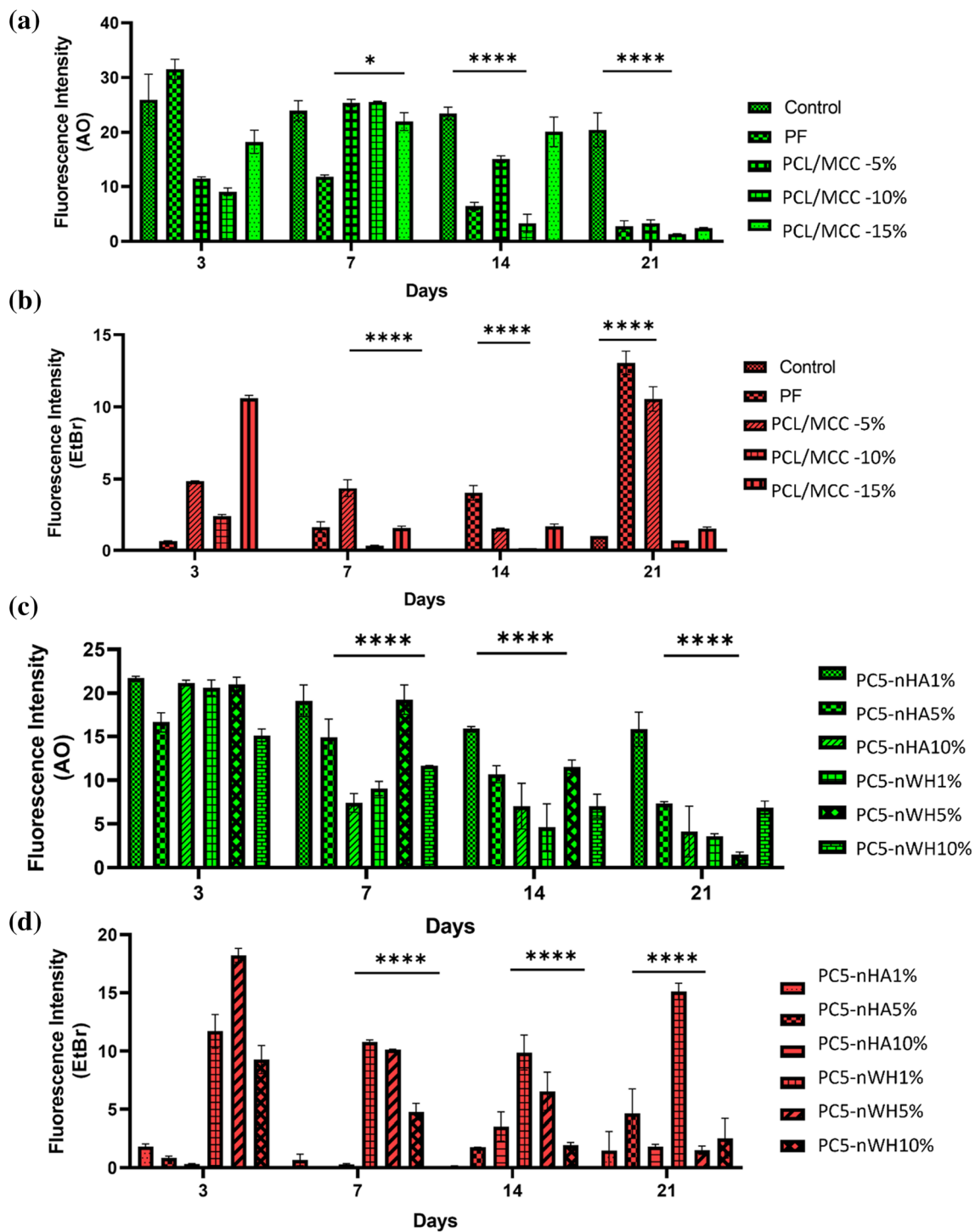


Fig. 10 Live Dead Assay quantitative analysis of NIH3T3-L1 cell lines for day 3, 7, 14, and 21. **a** LIVE cells for PCL/MCC composite, **b** DEAD cells for PCL/MCC composite, **c** LIVE cells for PC5/nHA

and PC5/nWH **d** DEAD cells for PC5/nHA and PC5/nWH. Data is statistically significant (Error bars: \pm SD, *p b 0.05, **p b 0.01, ***p b 0.001)

pattern, and DSC revealed that MCC addition upto 5wt% increased crystallinity of the composites nHA and nWH addition in PCL-MCC5 further increased crystallinity of the composites with increasing concentration of nanoparticles.

Mechanical properties of the composites were dramatically increased upon the addition of MCC upto 5wt%, nHA and nWH. nWH containing nanocomposites showed enhanced tensile strength compared to virgin PCL. Improvement in

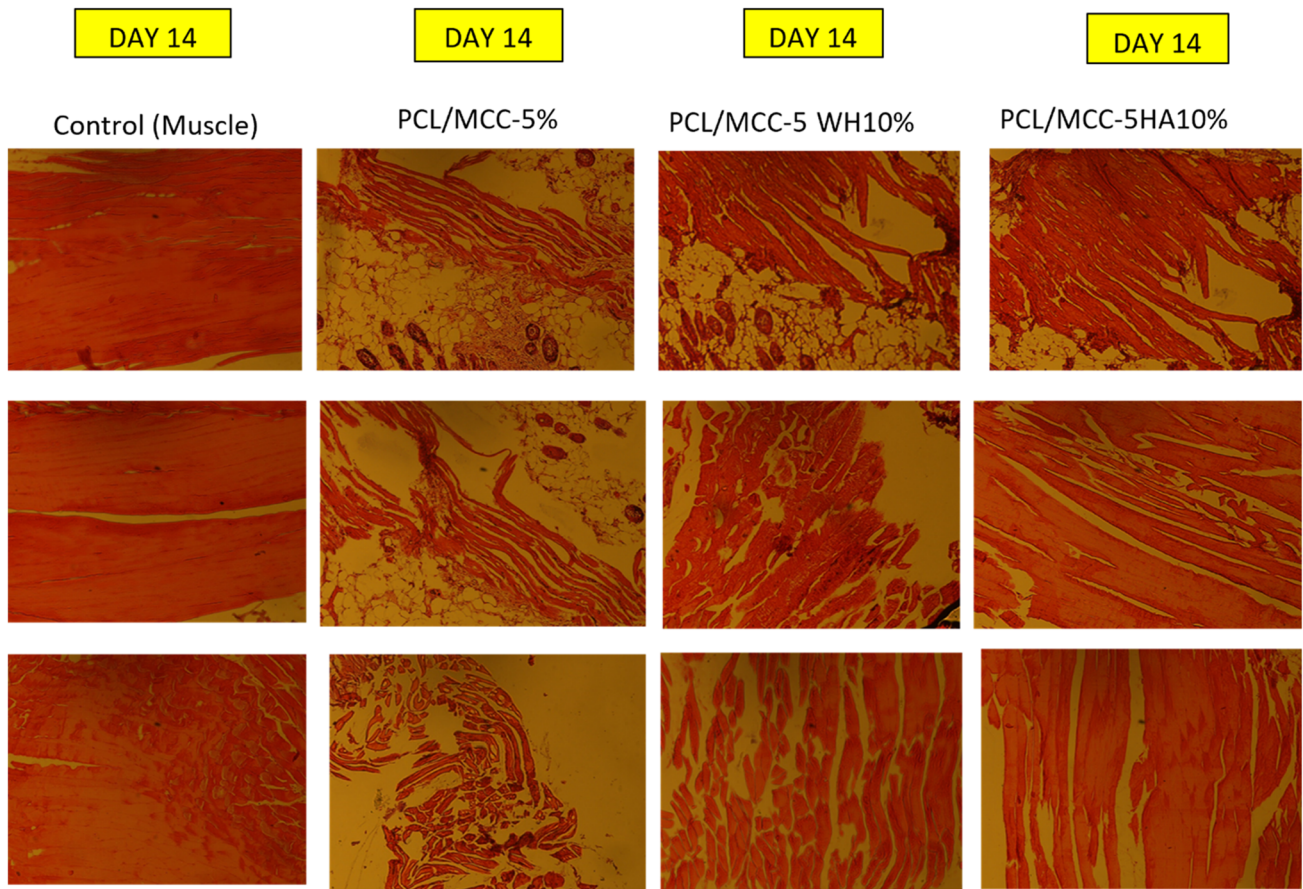


Fig. 11 Histological examination of bio interfacial affinity in the muscle tissue surrounding the implants after implantation for 2 weeks

the strength and stiffness of the hybrid nanocomposites was attributed to the increased crystallinity of the composites, enhanced mechanical properties is the prerequisite of sample fidelity. The bioactivity of the composites was studied on Vero and NIH3T3-L1 cell lines for days 3, 7, 14, and 21. The nanocomposites containing nHA and nWH showed improved cell adhesion compared to the PCL/MCC-5 composite, which implies that functional moieties of the nHA/nWH breed anchoring sites for the cell adhesion, which is required for forming the interconnected cellular network of bone. nHA and nWH addition in PCL-MCC5 improved osteoconductive and osteoinductivity of the composites. In vivo trials of nHA at 10% in PCL/MCC-5 composite demonstrated concentrated and thick muscle adherence and bio-interfacial affinity. These results suggest that MCC reinforced PCL biomimetic scaffold containing nHA and nWH can be used as a promising bone scaffold.

Acknowledgements The authors thank Department of Chemistry, School of Natural Sciences, National University of Sciences and Technology (NUST), Islamabad, Pakistan for the facilitation of characterization. We are thankful School of Biological Sciences, University of the Punjab, Lahore, Pakistan for providing cell culture facilities.

Author Contributions Conceptualization, FN, and MI; methodology, FN, and MI; software, FN, and LA; writing—original draft preparation, FN, LA, and MI; writing—review and editing, FN and LA, MI supervision, MI, and cell culture work, AT. All authors have read and agreed to the published version of the manuscript.

Funding This research received no external funding.

Declarations

Conflict of interest The authors declare no conflict of interest.

References

1. Ishman SL, Friedland DR (2004) Temporal bone fractures: traditional classification and clinical relevance. *Laryngoscope* 114:1734–1741
2. Roberts TT, Rosenbaum AJ (2012) Bone grafts, bone substitutes and orthobiologics: the bridge between basic science and clinical advancements in fracture healing. *Organogenesis* 8:114–124
3. Yu X, Yao S, Chen C, Wang J, Li Y, Wang Y, Khademhosseini A, Wan J, Wu Q (2020) Preparation of poly (ether-ether-ketone)/nanohydroxyapatite composites with improved mechanical performance and biointerfacial affinity. *ACS Omega* 5:29398–29406

4. Shuai C, Yu L, Feng P, Gao C, Peng S (2020) Interfacial reinforcement in bioceramic/biopolymer composite bone scaffold: the role of coupling agent. *Colloids Surf B* 193:111083
5. Prasadh S, Wong RCW (2018) Unraveling the mechanical strength of biomaterials used as a bone scaffold in oral and maxillofacial defects. *Oral Sci Int* 15:48–55
6. Morouço P, Biscaia S, Viana T, Franco M, Malça C, Mateus A, Moura C, Ferreira FC, Mitchell G, Alves NM (2016) Fabrication of poly (-caprolactone) scaffolds reinforced with cellulose nanofibers, with and without the addition of hydroxyapatite nanoparticles. *BioMed Res Int*. <https://doi.org/10.1155/2016/1596157>
7. Youseflee P, Ranjbar FE, Bahraminasab M, Ghanbari A, Faradonbeh DR, Arab S, Alizadeh A, Nooshabadi VT (2022) Exosome loaded hydroxyapatite (HA) scaffold promotes bone regeneration in calvarial defect: an in vivo study. *Cell Tissue Bank*. <https://doi.org/10.1007/s10561-022-10042-4>
8. Black CR, Goriainov V, Gibbs D, Kanczler J, Tare RS, Oreffo RO (2015) Bone tissue engineering. *Curr Mol Biol Rep* 1:132–140
9. Nazir F, Iqbal M, Khan AN, Mazhar M, Hussain Z (2021) Fabrication of robust poly L-lactic acid/cyclic olefinic copolymer (PLLA/COC) blends: study of physical properties, structure, and cytocompatibility for bone tissue engineering. *J Mater Res Technol* 13:1732–1751
10. Nazir F, Iqbal M (2021) Comparative study of crystallization, mechanical properties, and in vitro cytotoxicity of nanocomposites at low filler loadings of hydroxyapatite for bone-tissue engineering based on poly (L-lactic acid)/cyclo olefin copolymer. *Polymers* 13:3865
11. Aghajani MH, Panahi-Sarmad M, Alikarami N, Shojaei S, Saeidi A, Khonakdar HA, Shahravan M, Goodarzi V (2020) Using solvent-free approach for preparing innovative biopolymer nanocomposites based on PGS/gelatin. *Eur Polymer J* 131:109720
12. Nazir F, Iqbal M (2022) Piezoelectric MoS₂ nanoflowers (NF's) for targeted cancer therapy by gelatin-based shear thinning hydrogels. In vitro and in vivo trials. *React Funct Polym* 181:105435
13. Nazir F, Abbas L, Iqbal M (2022) A comparative insight into the mechanical properties, antibacterial potential, and cytotoxicity profile of nano-hydroxyapatite and nano-whitlockite-incorporated poly-L-lactic acid for bone tissue engineering. *Appl Nanosci* 12:47–68
14. Nazir F, Ashraf I, Iqbal M, Ahmad T, Anjum S (2021) 6-deoxyaminocellulose derivatives embedded soft gelatin methacryloyl (GelMA) hydrogels for improved wound healing applications: in vitro and in vivo studies. *Int J Biol Macromol* 185:419–433
15. Abrisham M, Noroozi M, Panahi-Sarmad M, Arjmand M, Goodarzi V, Shakeri Y, Golbaten-Mofrad H, Dehghan P, Sahzabi AS, Sadri M (2020) The role of polycaprolactone-triol (PCL-T) in biomedical applications: a state-of-the-art review. *Eur Polymer J* 131:109701
16. Rostamian M, Kalae MR, Dehkordi SR, Panahi-Sarmad M, Targar M, Goodarzi V (2020) Design and characterization of poly (glycerol-sebacate)-co-poly (caprolactone)(PGS-co-PCL) and its nanocomposites as novel biomaterials: the promising candidate for soft tissue engineering. *Eur Polymer J* 138:109985
17. Ebrahimi Z, Irani S, Ardeshirylajimi A, Seyedjafari E (2022) Enhanced osteogenic differentiation of stem cells by 3D printed PCL scaffolds coated with collagen and hydroxyapatite. *Sci Rep* 12:1–15
18. Ou S-F, Chiou S-Y, Ou K-L (2013) Phase transformation on hydroxyapatite decomposition. *Ceram Int* 39:3809–3816
19. Mohammadalazadeh Z, Bahremandi-Toloue E, Karbasi S (2022) Recent advances in modification strategies of pre-and post-electrospinning of nanofiber scaffolds in tissue engineering. *React Funct Polym* 172:105202
20. Alemán-Domínguez ME, Ortega Z, Benítez AN, Monzón M, Wang L, Tamaddon M, Liu C (2020) Microcrystalline cellulose as filler in polycaprolactone matrices, industry 4.0—shaping the future of the digital world. CRC Press, Boca Raton, pp 240–245
21. Janmohammadi M, Nazemi Z, Salehi AOM, Seyfoori A, John JV, Nourbakhsh MS, Akbari M (2023) Cellulose-based composite scaffolds for bone tissue engineering and localized drug delivery. *Bioactive Mater* 20:137–163
22. Hosseini H, Teymouri M, Saboor S, Khalili A, Goodarzi V, Hajipoor FP, Khonakdar HA, Shojaei S, Asefnejad A, Bagheri H (2019) Challenge between sequence presences of conductive additives on flexibility, dielectric and supercapacitance behaviors of nanofibrillated template of bacterial cellulose aerogels. *Eur Polymer J* 115:335–345
23. Saeedi M, Vahidi O, Goodarzi V, Saeb MR, Izadi L, Mozafari M (2017) A new prospect in magnetic nanoparticle-based cancer therapy: taking credit from mathematical tissue-mimicking phantom brain models. *Nanomed: Nanotechnol, Biol Med* 13:2405–2414
24. Panahi-Sarmad M, Abrisham M, Noroozi M, Goodarzi V, Arjmand M, Sadri M, Dehghan P, Amirikiai A, Khonakdar HA (2020) Programming polyurethane with rational surface-modified graphene platelets for shape memory actuators and dielectric elastomer generators. *Eur Polymer J* 133:109745
25. Nemati-Kande E, Karimian R, Goodarzi V, Ghazizadeh E (2020) Feasibility of pristine, Al-doped and Ga-doped Boron Nitride nanotubes for detecting SF₄ gas: a DFT, NBO and QTAIM investigation. *Appl Surf Sci* 510:145490
26. Hosseini H, Zirakjou A, McClements DJ, Goodarzi V, Chen W-H (2022) Removal of methylene blue from wastewater using ternary nanocomposite aerogel systems: carboxymethyl cellulose grafted by polyacrylic acid and decorated with graphene oxide. *J Hazard Mater* 421:126752
27. Lughmani F, Nazir F, Khan SA, Iqbal M (2022) Novel functionalized cellulose derivatives fabricated with Cu nanoparticles: synthesis, characterization and degradation of organic pollutants. *Cellulose* 29:1911–1928
28. Rostamian M, Hosseini H, Fakhri V, Talouki PY, Farahani M, Gharehtzpeh AJ, Goodarzi V, Su C-H (2022) Introducing a bio sorbent for removal of methylene blue dye based on flexible poly (glycerol sebacate)/chitosan/graphene oxide ecofriendly nanocomposites. *Chemosphere* 289:133219
29. Hosseini H, Pirahmadi P, Shakeri SE, Khoshbakhti E, Sharafkhani S, Fakhri V, Saeidi A, McClements DJ, Chen W-H, Su C-H (2022) A novel environmentally friendly nanocomposite aerogel based on the semi-interpenetrating network of polyacrylic acid into Xanthan gum containing hydroxyapatite for efficient removal of methylene blue from wastewater. *Int J Biol Macromol* 201:133–142
30. Arokiasamy P, Abdullah MMAB, Abd Rahim SZ, Luhar S, Sandu AV, Jamil NH, Nabialek M (2022) Synthesis methods of hydroxyapatite from natural sources: a review. *Ceram Int* 48:14959–14979
31. Kaliannagounder VK, Raj NPMJ, Unnithan AR, Park J, Park SS, Kim S-J, Park CH, Kim CS, Sasikala ARK (2021) Remotely controlled self-powering electrical stimulators for osteogenic differentiation using bone inspired bioactive piezoelectric whitlockite nanoparticles. *Nano Energy* 85:105901
32. Capitelli F, Bosi F, Capelli SC, Radica F, Della Ventura G (2021) Neutron and XRD single-crystal diffraction study and vibrational properties of whitlockite, the natural counterpart of synthetic tricalcium phosphate. *Crystals* 11:225
33. Wang C, Jeong K-J, Park HJ, Lee M, Ryu S-C, Hwang DY, Nam KH, Han IH, Lee J (2020) Synthesis and formation mechanism of bone mineral, whitlockite nanocrystals in tri-solvent system. *J Colloid Interface Sci* 569:1–11
34. Cooper MA, Hawthorne FC, Abdu YA, Ball NA, Ramik RA, Tait KT (2013) Wopmayite, ideally Ca₆Na₃ Mn (PO₄)₃ (PO₃OH)₄, a new phosphate mineral from the Tanco Mine, Bernic Lake, Manitoba: description and crystal structure. *Can Mineral* 51:93–106
35. Fujii E, Kawabata K, Nakazaki Y, Tanizawa Y, Shirosaki Y, Hayakawa S, Osaka A (2011) Fabrication of hydroxyapatite

- with controlled morphology in a micro-reactor. *J Ceram Soc Jpn* 119:116–119
36. Klinkaewnarong J, Utara S (2018) Ultrasonic-assisted conversion of limestone into needle-like hydroxyapatite nanoparticles. *Ultrason Sonochem* 46:18–25
 37. Rajabnejadkeleshteri A, Kamyar A, Khakbiz M, Basiri H (2020) Synthesis and characterization of strontium fluor-hydroxyapatite nanoparticles for dental applications. *Microchem J* 153:104485
 38. Fernández MD, Guzmán DJ, Ramos JR, Fernández MJ (2019) Effect of alkyl chain length in POSS nanocage on non-isothermal crystallization behavior of PCL/amino-POSS nanocomposites. *Polymers* 11:1719
 39. Nasrollahi F, Nazir F, Tavafoghi M, Hosseini V, Ali Darabi M, Parmelle D, Khademhosseini A, Ahadian S (2021) Graphene quantum dots for fluorescent labeling of gelatin-based shear-thinning hydrogels. *Adv NanoBiomed Res* 1:2000113
 40. Ain QU, Khan AN, Nabavinia M, Mujahid M (2017) Enhanced mechanical properties and biocompatibility of novel hydroxyapatite/TOPAS hybrid composite for bone tissue engineering applications. *Mater Sci Eng: C* 75:807–815
 41. Gergely G, Wéber F, Lukács I, Tóth AL, Horváth ZE, Mihály J, Balázs C (2010) Preparation and characterization of hydroxyapatite from eggshell. *Ceram Int* 36:803–806
 42. Jang HL, Jin K, Lee J, Kim Y, Nahm SH, Hong KS, Nam KT (2014) Revisiting whitlockite, the second most abundant biomineral in bone: nanocrystal synthesis in physiologically relevant conditions and biocompatibility evaluation. *ACS Nano* 8:634–641
 43. Arrieta MP, Leonés Gil A, Yusef M, Kenny JM, Peponi L (2020) Electrospinning of PCL-based blends: processing optimization for their scalable production. *Materials* 13:3853
 44. Nazir F, Iqbal M (2020) Synthesis, characterization and cytotoxicity studies of aminated microcrystalline cellulose derivatives against melanoma and breast cancer cell lines. *Polymers* 12:2634
 45. dos Santos FA, Iulianelli GC, Tavares MI (2017) Effect of microcrystalline and nanocrystals cellulose fillers in materials based on PLA matrix. *Polym Test* 61:280–288
 46. Gieroba B, Przekora A, Kalisz G, Kazimierzczak P, Song CL, Wojcik M, Ginalska G, Kazarian SG, Sroka-Bartnicka A (2021) Collagen maturity and mineralization in mesenchymal stem cells cultured on the hydroxyapatite-based bone scaffold analyzed by ATR-FTIR spectroscopic imaging. *Mater Sci Eng: C* 119:111634
 47. Panda S, Biswas CK, Paul S (2021) A comprehensive review on the preparation and application of calcium hydroxyapatite: a special focus on atomic doping methods for bone tissue engineering. *Ceram Int* 47:28122–28144
 48. Alemán-Domínguez ME, Giusto E, Ortega Z, Tamaddon M, Benitez AN, Liu C (2019) Three-dimensional printed polycaprolactone-microcrystalline cellulose scaffolds. *J Biomed Mater Res Part B: Appl Biomater* 107:521–528
 49. Gómez-Lizárraga K, Flores-Morales C, Del Prado-Audelo M, Álvarez-Pérez M, Piña-Barba M, Escobedo C (2017) Polycaprolactone-and polycaprolactone/ceramic-based 3D-bioplotted porous scaffolds for bone regeneration: a comparative study. *Mater Sci Eng: C* 79:326–335
 50. Simao JA, Bellani CF, Branciforti MC (2017) Thermal properties and crystallinity of PCL/PBSA/cellulose nanocrystals grafted with PCL chains. *J Appl Polymer Sci*. <https://doi.org/10.1002/app.44493>
 51. Ruseckaite RA, Jiménez A (2003) Thermal degradation of mixtures of polycaprolactone with cellulose derivatives. *Polym Degrad Stab* 81:353–358
 52. Karimian R, Mehrabani MG, Mehramuz B, Ganbarov K, Ejlali L, Tanomand A, Kamounah FS, Rezaee MA, Yousefi M, Sheykhsaran E (2020) Poly (*e*-Caprolactone)/cellulose nanofiber blend nanocomposites containing ZrO₂ nanoparticles: a new biocompatible wound dressing bandage with antimicrobial activity. *Adv Pharm Bull* 10:577
 53. Jarcho M, Salsbury R, Thomas M, Doremus R (1979) Synthesis and fabrication of β -tricalcium phosphate (whitlockite) ceramics for potential prosthetic applications. *J Mater Sci* 14:142–150
 54. Cocca M, Avolio R, Gentile G, Di Pace E, Errico M, Avella M (2015) Amorphized cellulose as filler in biocomposites based on poly (ϵ -caprolactone). *Carbohydr Polym* 118:170–182
 55. Mi H-Y, Jing X, Peng J, Salick MR, Peng X-F, Turng L-S (2014) Poly (*e*-caprolactone)(PCL)/cellulose nano-crystal (CNC) nanocomposites and foams. *Cellulose* 21:2727–2741
 56. Celebi H, Ilgar M, Seyhan AT (2022) Evaluation of the effect of isocyanate modification on the thermal and rheological properties of poly (*e*-caprolactone)/cellulose composites. *Polym Bull* 79:4941–4955
 57. Chen J, Xu C, Wu D, Pan K, Qian A, Sha Y, Wang L, Tong W (2015) Insights into the nucleation role of cellulose crystals during crystallization of poly (β -hydroxybutyrate). *Carbohydr Polym* 134:508–515
 58. Eftekhari S, El Sawi I, Bagheri ZS, Turcotte G, Bougherara H (2014) Fabrication and characterization of novel biomimetic PLLA/cellulose/hydroxyapatite nanocomposite for bone repair applications. *Mater Sci Eng: C* 39:120–125
 59. Hickey DJ, Ercan B, Sun L, Webster TJ (2015) Adding MgO nanoparticles to hydroxyapatite–PLLA nanocomposites for improved bone tissue engineering applications. *Acta Biomater* 14:175–184
 60. Guo Z, Yang C, Zhou Z, Chen S, Li F (2017) Characterization of biodegradable poly (lactic acid) porous scaffolds prepared using selective enzymatic degradation for tissue engineering. *RSC Adv* 7:34063–34070
 61. Gaharwar AK, Dammu SA, Canter JM, Wu C-J, Schmidt G (2011) Highly extensible, tough, and elastomeric nanocomposite hydrogels from poly (ethylene glycol) and hydroxyapatite nanoparticles. *Biomacromolecules* 12:1641–1650
 62. Koupaei N, Karkhaneh A, Joupri MD (2015) Preparation and characterization of (PCL-crosslinked-PEG)/hydroxyapatite as bone tissue engineering scaffolds. *J Biomed Mater Res Part A* 103:3919–3926
 63. Passos MF, Fernández-Gutiérrez M, Vázquez-Lasa B, San Román J, Maciel Filho R (2016) PHEMA-PLLA semi-interpenetrating polymer networks: a study of their swelling kinetics, mechanical properties and cellular behavior. *Eur Polymer J* 85:150–163
 64. Zhu Y, Sheng Y, Zheng L, Qin L, Ngai T (2019) Poly (l-lactic acid) (PLLA) Coatings with controllable hierarchical porous structures on magnesium substrate: an evaluation of corrosion behavior and cytocompatibility. *ACS Appl Bio Mater* 2:3843–3853
 65. Hickey DJ (2014) MgO nanocomposites as antibacterial biomaterials for orthopedic tissue engineering. Northeastern University, Boston
 66. Hickey DJ, Ercan B, Chung S, Webster TJ, Sun L, Geilich B (2014) MgO nanocomposites as new antibacterial materials for orthopedic tissue engineering applications, 40th Annual Northeast Bioengineering Conference (NEBEC), IEEE, pp. 1–2
 67. Yu X, Yao S, Chen C, Wang J, Li Y, Wang Y, Khademhosseini A, Wan J, Wu QJAO (2020) Preparation of poly (ether-ether-ketone)/nanohydroxyapatite composites with improved mechanical performance and biointerfacial affinity. *ACS Omega* 5:29398–29406

Publisher's Note Springer Nature remains neutral with regard to jurisdictional claims in published maps and institutional affiliations.

Springer Nature or its licensor (e.g. a society or other partner) holds exclusive rights to this article under a publishing agreement with the author(s) or other rightsholder(s); author self-archiving of the accepted manuscript version of this article is solely governed by the terms of such publishing agreement and applicable law.